

Structure and reactivity of oxalate surface complexes on lepidocrocite derived from infrared spectroscopy, DFT-calculations, adsorption, dissolution and photochemical experiments

Susan C. Borowski^a, Jagannath Biswakarma^{a,c}, Kyounglim Kang^b, Walter D.C. Schenkeveld^b, Janet G. Hering^{a,c,d}, James D. Kubicki^e, Stephan M. Kraemer^b, Stephan J. Hug^{a*}

^a Eawag, Swiss Federal Institute of Aquatic Science and Technology, Ueberlandstrasse 133, CH-8600 Duebendorf, Switzerland

^b University of Vienna, Dept. of Environmental Geosciences and Environmental Science Research Network, Althanstraße 14 (UZA II) 1090 Vienna, Austria

^c Swiss Federal Institute of Technology (ETH) Zürich, IBP, CH-8092 Zürich, Switzerland

^d Swiss Federal Institute of Technology Lausanne (EPFL), ENAC, CH-1015 Lausanne, Switzerland

^e The University of Texas at El Paso, Dept. of Geological Sciences, 500 West University Avenue, El Paso, TX 79968, USA

* Corresponding author. E-mail: stephan.Hug@eawag.ch

Current address of S.C. Borowski: Virginia Military Institute, Lexington, VA 24450, USA. E-mail: borowskisc@vmi.edu

Abstract

Oxalate, together with other ligands, plays an important role in the dissolution of iron(hydr)oxides and the bio-availability of iron. The formation and properties of oxalate surface complexes on lepidocrocite were studied with a combination of infrared spectroscopy (IR), density functional theory (DFT) calculations, dissolution, and photochemical experiments. IR spectra measured as a function of time, concentration, and pH (50-200 μ M oxalate, pH 3-7) showed that several surface complexes are formed at different rates and in different proportions. Measured spectra could be separated into three contributions described by Gaussian line shapes, with frequencies that agreed well with the theoretical frequencies of three different surface complexes: an outer-sphere complex (OS), an inner-sphere monodentate mononuclear complex (MM), and a bidentate mononuclear complex (BM) involving one O atom from each carboxylate group. At pH 6, OS was formed at the highest rate. The contribution of BM increased with decreasing pH. In dissolution experiments, lepidocrocite was dissolved at rates proportional to the surface concentration of BM, rather than to the total adsorbed concentration. Under UV-light (365 nm), BM was photolyzed at a higher rate than MM and OS. Although the comparison of measured spectra with calculated frequencies cannot exclude additional possible structures, the combined results allowed the assignment of three main structures with different reactivities consistent with experiments. The results illustrate the importance of the surface speciation of adsorbed ligands in dissolution and photochemical reactions.

1. INTRODUCTION

Oxalate is formed and consumed in numerous biotic and abiotic processes and occurs in micro- to millimolar concentrations in soil porewater, DOC-rich surface waters, and in aerosols. In the pH range from 3 to 7, oxalate adsorbs strongly to mineral oxide surfaces and affects the surface properties and the dissolution rates of minerals. Of particular importance is the role of oxalate in the dissolution of Fe-containing minerals, which influences the bio-availability of Fe in soils, surface water, and the ocean. Oxalate can promote the dissolution in non-reductive and reductive reactions (Banwart et al., 1989; Cheah et al., 2003; Kraemer, 2004; Loring et al., 2008; Reichard et al., 2007), and in light-induced reactions (Cwiertny et al., 2009; Deutsch et al., 2001; Sulzberger and Laubscher, 1995). The formation, structure and properties of oxalate surface complexes on iron(hydr)oxide phases are thus of continued interest.

Several studies have addressed the adsorption and the structure of oxalate surface complexes on metal (hydr)oxide (MHO) and specifically on iron(hydr)oxide mineral surfaces with spectroscopic methods, particularly with infrared (IR) spectroscopy. With the progress of computational methods, results of spectroscopic studies can be compared to computational results of increasingly realistic representations of MHO-surface sites with oxalate adsorbed in various possible structures, including the presence of water. A complicating factor is that measured infrared spectra are often the sum of contributions from several surface complexes. Most studies, both experimental and theoretical, agree that oxalate can form several different surface complexes on each investigated MHO. However, a consistent view on the adsorption mechanisms and the contributions of various complexes and their structures is still missing. Outer-sphere (OS), hydrogen-bonded outer-sphere (HOS), and several inner-sphere complexes, such as monodentate-mononuclear (MM), bidentate-mononuclear (BM), bidentate-binuclear (BB), and differently protonated structures can contribute to observed spectra. In the following, we briefly review the findings of previous studies.

In one of the first studies applying Attenuated Total Reflectance Fourier Transform Infrared spectroscopy (ATR-FTIR) with metal-oxide coated ATR-elements, the adsorption of oxalate to TiO_2 was studied as a function of concentration and pH (1-1000 μM oxalate, pH 2.9-8.6) (Hug and Sulzberger, 1994). It was found that several different surface complexes are formed as a function of aqueous concentration and pH. The authors suggested that inner-sphere BM and/or BB structures and a protonated surface complex are formed, but a comparison with molecular orbital (MO) calculations could not be performed at that time. A series of subsequent ATR-FTIR studies addressing the adsorption of oxalate as function of pH, concentration and time (without MO-calculations) found further evidence for the formation of several surface complexes. Degenhardt and McQuillan measured the pH-dependence and kinetics of the adsorption of oxalate (0-1 mM oxalate, pH 3) on amorphous $\text{Cr(III)(hydr)oxide}$ and suggested a fast formation of ionic (OS), and hydrogen-bonded oxalate (HOS), followed by a slower formation of coordinated oxalate with BM or BB structures (Degenhardt and McQuillan, 1999). They suggested that at low pH, protonation and breaking of Cr-O-Cr linkages could lead to more sorption sites, which could explain the slowly increasing contribution of the spectrum of coordinated oxalate. Later, Young and McQuillan followed the adsorption/desorption kinetics of oxalate at the TiO_2 interface at pH 4.0 with 100 μM oxalate. An analysis of the desorption kinetics yielded three different rate constants, each corresponding to the desorption of a different surface complex (Young and McQuillan, 2009). The most slowly desorbing complex was the one with a spectral signature consistent with a BM or BB structure, the least stable was the OS complex. Hug and Bahnemann measured and compared IR-spectra of oxalate, malonate and succinate adsorbed on anatase, rutile and lepidocrocite, as a function of pH (3-9) at 200 μM aqueous concentrations of the dicarboxylates (Hug and Bahnemann, 2006). The spectra of each ligand exhibited distinct differences on the different oxides. A qualitative interpretation of spectra lead to the conclusion that oxalate formed five or six-member chelate ring structures (BM or BB, respectively) involving one O from each carboxylic group and that multiple complexes were formed at each surface. Loring et al. followed the adsorption of oxalate [ca. 1 $\mu\text{mol/m}^2$] with ATR-FTIR over a timescale of days (Loring et al., 2008). They observed initial formation of outer- and inner-sphere

surfaces complexes, followed by formation of a pool of tris-oxalate that remained adsorbed on the surface at pH 4, and which was then quickly dissolved upon addition of deferroxamine (DFOB). It was suggested that OS and BM surface complexes are formed quickly, followed by slow formation of adsorbed Fe(III)-tris-oxalato complexes. Simanova et al. measured the formation of oxalate surface complexes on goethite at pH 4 on a time scale from minutes to 2 days with an oxalate surface concentration of 1 $\mu\text{mol}/\text{m}^2$ (Simanova et al., 2011). The temporal evolution of the IR-spectra was explained with four coordination modes of oxalate: OS, HOS, BM, and inner-sphere with ternary-type complex (BM adsorption to Fe(III) adsorbed to the surface). Situm et al. studied the adsorption of citrate, oxalate and pyrocatechol on hematite nanoparticles with ATR-FTIR and found that oxalate formed deprotonated outer-sphere complexes with contributions from deprotonated inner-sphere complexes (Situm et al., 2016).

A group of more recent studies applied MO-calculations to interpret experimentally measured spectra. Persson and Axe investigated the adsorption of oxalate and malonate on goethite (0.7 and 1.4 $\mu\text{mol}/\text{m}^2$ oxalate, pH 2.5-8) (Persson and Axe, 2005) and suggested that oxalate and malonate form HOS and inner-sphere BM surface complexes on goethite. By comparing the IR-spectra of adsorbed oxalate to spectra of dissolved Fe-oxalate and to calculated IR-spectra (DFT using B3LYP functionals, standard 6-31+G basis set and Gaussian 98), they suggested that the surface complexes are five-membered ring BM structures. Mendive et al. studied oxalate complexes on the surface of rutile and anatase and compared experimental ATR-FTIR spectra (100-400 μM , pH 3.7) with theoretical predictions of semi-empirical (MSINDO) calculations (Mendive et al., 2009). These authors found evidence for three different surface complexes on rutile and four complexes on anatase and suggested that bidentate complexes are more stable than monodentate complexes. Bhandari et al. studied the adsorption of oxalate on ferrihydrite (FH) and the photodissolution of FH upon irradiation with light from a high-pressure xenon lamp (Bhandari et al., 2010). IR-spectra were measured at pH 4.5 and with 5 mM aqueous oxalate concentrations. Adsorption from 0-30 min showed an evolution to a final spectrum, from which the following peak positions were determined: 1708 cm^{-1} [$\nu_s(\text{C}=\text{O})$], 1668 cm^{-1} [$\nu_a(\text{C}=\text{O})$], 1412 cm^{-1} [$\nu_s(\text{C}-\text{O})$ and $\nu(\text{C}-\text{C})$ combination mode] and 1280 cm^{-1} [$\nu_a(\text{C}-\text{O})$]. The structure of adsorbed oxalate was derived by comparison of measured spectra with frequencies obtained from DFT-calculations (Gaussian 03E.0126 at the B3LYP/6-31G level). They concluded that a BM structure was most likely, while an MM structure showed a slightly worse agreement with the experimental peak positions. Their spectra are in agreement with the observations and interpretations of Hug and Bahnemann (Hug and Bahnemann, 2006),.

In summary, all previous studies concluded that oxalate forms more than one surface complex structure at the investigated MHO surfaces and that the inner-sphere complexes are BM or BB structures. However, a convincing separation of experimentally observed spectral contributions into spectra of different surface complexes and their comparison with calculated spectra is still missing.

The aim of this study was the separation of spectra from different surface complexes and the determination of their structure by comparison with calculated spectra. A second aim was to assess the reactivity of the different surface complexes. We thus investigated the adsorption of oxalate to lepidocrocite in more detail by comprehensive measurements, in combination with state-of-the art density function theory (DFT) calculations with solvated periodic structures and representative molecular clusters. Lepidocrocite ($\gamma\text{-FeOOH}$, space group Pnma) was chosen for its importance in various aqueous environments and its higher reactivity in dissolution reactions compared to hematite and goethite. A detailed knowledge about the pH-dependent formation and structure of surface complexes of oxalate is a prerequisite for the understanding of the effects of oxalate on the dissolution of iron oxides. IR-spectra contain detailed structural information, but the separation of observed spectral contributions into spectra of different surface complexes and their structural interpretation is challenging. Adsorption and photochemical experiments were designed to allow for a separation of different spectral contributions and to find the most consistent agreement between separated measured and calculated spectra. To derive more generally valid conclusions for lepidocrocite, we conducted experiments with two morphologically different samples of synthetic lepidocrocite.

2. MATERIALS AND METHODS

2.1. Materials

Two types of lepidocrocite were used, in the following abbreviated with **Lp-1** and **Lp-2**. **Lp-1** was synthesized according the method of [Brauer \(1963\)](#), as described in detail in Borer et al. (Borer et al., 2009) and had a specific surface area of 130 m²/g (determined by the multipoint N₂-Brunauer-Emmett-Teller (BET) method. **Lp-2** was synthesized according to the method of Schwertmann et al. ([Schwertmann and Cornell, 2000](#)) and had a specific BET surface area of 63 m²/g. Purity and crystallinity was confirmed by X-ray powder diffraction analysis. Oxalic acid dihydrate (C₂H₂O₄·2H₂O, Sigma-Aldrich, > 99%), sodium chloride (NaCl, Merck, > 99%), piperazine-1,4-bis-(propane-sulfonic acid) (PIPPS, C₁₀H₂₂N₂O₆S₂, pK_a = 3.73, Merck), 1,4-dimethylpiperazine (DEPP, C₆H₁₄N₂, pK_a = 4.48, Sigma-Aldrich, >98%), 2-morpholinoethanesulfonic acid monohydrate (MES, C₆H₁₃NO₄S·H₂O, pK_a = 6.06, Merck, >99%) were used as received without further purification. Ultrapure water (resistivity > 18.2 MΩ·cm, TOC > 2 ppb, Milli-Q, Millipore) was used in all experiments.

2.2. FTIR Measurements

Infrared spectra (4000-400 cm⁻¹, 2 cm⁻¹ resolution, 32 or 64 scans) were recorded on a Biorad FTS 575C instrument equipped with a mercury cadmium telluride (MCT) detector and a 9-reflection ATR unit (SensIR Technologies, Danbury, CT), as described in detail previously ([Borer and Hug, 2014](#); [Borer et al., 2007](#); [Borer et al., 2009](#)). In brief, the circular (4 mm diameter) diamond surface of the ATR-unit was coated with 15-30 µg lepidocrocite (both for Lp-1 and Lp-2). Subsequently a liquid cell assembly was mounted on the ATR-plate and the layer was immersed in aqueous solution (10-40 ml of 10 mM NaCl inert electrolyte). Once the signal was stable, a single beam spectrum was recorded, which served as the background for the calculation of subsequent absorbance spectra. The liquid was purged with N₂, which lead to desorption of adsorbed CO₂. (Spectra of a lepidocrocite layer and difference spectra during desorption of CO₂ are shown in [Figures EA1A and EA1B](#)). A new background spectrum was measured after the signal was stable, before 200 µM oxalate was added. Adsorption kinetics and pH-dependent spectra were measured by changing and adjusting the pH with 0.1 M HCl and NaOH. The spectra of dissolved oxalic acid and oxalate were measured by titrating a 50 mM oxalic acid solution in contact with the uncoated ATR-diamond surface with 1 M NaOH (the background single beam spectrum was that of pure H₂O). These spectra were corrected for the slight dilution by addition of NaOH. Spectra of Fe-oxalate complexes were measured with 1:1, 1:2 and 1:3 mixtures of FeCl₃ and oxalate (10 mM FeCl₃ and 10-30 mM oxalate in H₂O and 50 mM FeCl₃ and 50 mM oxalate in D₂O, respectively). Photochemical experiments were conducted with 1.0 ml of 200 µM pH 4.0 oxalate solution, covered with a UV-transparent glass plate. After a stable adsorption plateau had been reached (30 min), the lepidocrocite layer was illuminated with a UV-LED lamp (Dr. Groebel UVElektronik GmbH, Ettlingen, Germany, 365 ± 5 nm) at 3.25 cm distance above the layer. The photon flux, measured by ferrioxalate actinometry, was 2±0.3 µmol photons/min (corresponding to 960 W/m²) at the oxide layer, approximately 9-fold the irradiance of natural sunlight in the range of 300–450 nm. For more details see (Borer and Hug, 2014). In all FTIR non-photochemical experiments described here, oxalate in solution (40 ml of 200 µM = 8.0 µMol) was in large excess over lepidocrocite (30µg) available surface sites (e.g. 15.7 nMol surface sites for Lp-2, assuming 5 sites/nm²). Thus, oxalate concentrations did not change during the experiments and the oxalate surface concentrations were those in equilibrium with 200 µM aqueous oxalate. This concentration can occur in soils and atmospheric water, does not lead to an untypical oversaturation of the surface, and is in the range of previously conducted and published studies.

2.3. Dissolution and adsorption experiments

2.3.1 Oxalate promoted dissolution of lepidocrocite

The dissolution of **Lp-2** was observed under ambient air at constant temperature ($20\pm1^\circ\text{C}$). All experiments were performed in 100 mL LDPE reactors. The reactors were wrapped in aluminum foil to prevent potential photo-reductive reactions. The lepidocrocite suspensions were completely mixed with a magnetic stirrer and a Teflon-coated stirring bar. The ionic strength was fixed with 0.01 M NaCl. The pH was adjusted with HCl or NaOH solutions and buffered at pH values between 4 and 6 (± 0.05) with 0.005 M of PIPPS (pH 4 and 4.5), DEPP (pH 5 and 5.5) or MES (pH 6). Lepidocrocite suspensions were equilibrated overnight prior to oxalate addition at 90% of the final solution volume in ambient air. Oxalate was added to a concentration of 500 μM and the lepidocrocite suspensions density was set to 0.1 g L^{-1} . Suspension samples were taken periodically and filtered over 0.1 μm pore sized polyvinylidene fluoride (PDVF) syringe filter (SLVV033RS, Merck). Sampling frequency depended on the pH. Samples were acidified with trace metal grade nitric acid (Fisher) and the total dissolved Fe concentration was determined by inductively coupled plasma mass spectrometry (ICP-MS, Agilent 7700).

2.3.2 Adsorption of oxalate on lepidocrocite

Adsorption experiments with oxalate and 1 g L^{-1} **Lp-2** were conducted for the pH range pH 4 to pH 6 at an ionic strength corresponding to the dissolution experiments. The suspension pH values were set using HNO_3 and NaOH solutions and the suspensions were equilibrated overnight prior to oxalate addition at 90% of the final solution volume in ambient air. Oxalate was added to the lepidocrocite suspension to a concentration of 500 μM and equilibrated for 1 min. In order to prevent a pH drift due to co-adsorption of protons to the lepidocrocite surface, HNO_3 solution was added, and the suspension pH were stable during the reaction time (± 0.05). The interaction time was set to minimize lepidocrocite dissolution, but still approach adsorption equilibrium. The total dissolved iron concentrations after the interaction time were measured by ICP-MS. Dissolved iron as iron-oxalate complexes accounted for less than 2 percent of the applied amount of oxalate. We expect that adsorption of iron-oxalate complexes is minimal under these conditions, but in the absence of adsorption measurements for such complexes their effect on oxalate surface speciation is not known. Samples were filtered over 0.1 μm pore sized PDVF syringe filter (SLVV033RS, Merck (0.1 μm)). The total dissolved oxalate concentration was analyzed by High-performance liquid chromatography (HPLC, Agilent 1260) using a ZORBAX SB-C18 ($4.6 \times 150 \text{ mm}$, 5 μm) column. A diode array detector (BIO Max-Light Cell 10 mm, G5615-60018, $\lambda = 210 \text{ nm}$) was connected to the HPLC. The mobile phase was composed of acetonitrile (CH_3CN , Merck, $>99.5 \%$) and water in a ratio of 50:50; the flow rate was set to 1 mL min^{-1} .

2.4. Computational methods

2.4.1. Model Construction

Periodic cells: Using Materials Studio 6.0, (Accelrys Software, 2007) models of the oxalate-lepidocrocite-water system were created by cleaving the respective surfaces – (010) and (100) – from the experimental crystal structure of bulk lepidocrocite (space group Pnma) through the plane breaking the fewest number of Fe–O bonds. Periodic models of the surfaces were created with a vacuum space of 20 Å between repeating lepidocrocite surfaces. Oxalate was added to the surface in both monodentate and bidentate configurations as guided by previous results on molecular clusters (Bhandari et al., 2010). Outer-sphere configurations were created with $\text{C}_2\text{O}_4^{2-}$. In order to mimic a “dry” surface, 36 and 32 H_2O molecules were added to the (010) and (100) models, respectively. To mimic a “solvated” surface, 125 and 95 H_2O molecules were added to the (010) and (100) models, respectively, representing a density of approximately 1 g/cm^3 . For the *dry* systems, two H^+ ions were added to random bi-coordinated O atoms of the lepidocrocite slabs to maintain an electrostatically

neutral simulation cell. For the *solvated* systems, two H⁺ ions were added to random H₂O molecules. The mineral slab of the periodic systems studied for the (010) system consisted of Fe₆₄O₁₂₈H₆₄, measuring 15.5 × 12.3 × 32.0 Å³, and the (100) system consisted of Fe₄₈O₁₂₀H₉₆ measuring 12.7 × 11.8 × 30.8 Å³. The magnetic ordering of the Fe atoms was set according to the experimentally-observed antiferromagnetic pattern (Coey et al., 1995; Cornell and Schwertmann, 2003) as described previously (Kubicki et al., 2008).

Molecular clusters: Upon completion of the energy minimizations of the periodic systems, molecular clusters were extracted. Each cluster was created by selecting the third nearest neighbors of the surface atoms bonded to the adsorbed oxalate, then expanded until eight Fe atoms were included. The Fe atoms were terminated with OH⁻ and H₂O groups, eliminating dangling bonds and maintaining overall charge neutrality. Additional H₂O molecules were added to hydrogen bond to the oxalate, yielding Fe₈O₄₂H₅₄C₂ clusters (exceptions noted).

2.4.2. Calculations with periodic cells

Projector-augmented plane-wave calculations (Blöchl, 1994; Kresse and Joubert, 1999) were performed using VASP 5.2, (Kresse and Furthmüller, 1996) using the generalized gradient approximation (GGA) PBE pseudopotentials (Perdew et al., 1997; Perdew et al., 1996) and Vanderbilt-type ultrasoft pseudopotentials (Laasonen et al., 1991) with an energy cutoff of 500 eV. The electron density cutoff was 1 × 10⁻⁴ eV. Partial occupancies were determined using the first-order scheme of the Methfessel–Paxton method with a 0.1 eV width. Initial magnetic moments of Fe atoms were assigned as alternate positive and negative values (± 5) on the crystalline layers along the Miller direction [010] so as to obtain an antiferromagnetic lepidocrocite slab in each case. The on-site Coulomb interaction, the GGA+U method, was applied to the Fe atoms according to the approach of Dudarev et al. as implemented in VASP (Dudarev et al., 1998). The supercell lattice parameters were held fixed throughout the simulations, but all atoms were allowed to relax without symmetry restrictions. A single *k*-point was evaluated at the Γ -point of the supercell, which provides acceptable energy results for such relatively large models. Each model was energy minimized; the ionic relaxations were considered to be converged when the change in the free energy of the system between two steps dropped below 1 × 10⁻² eV Å⁻¹.

2.4.3. Calculations with molecular clusters

Energy minimizations were performed in the gas-phase using Gaussian 09 (Frisch et al.) with all Fe atoms initially frozen and then allowed to relax. This stepwise energy minimization helps to ensure that the cluster model retains structural similarity to the original periodic surface configuration. Only high-spin complexes were analyzed. The B3LYP exchange-correlation functional (Becke, 1993; Lee et al., 1988) was used with the 6-31G(d,p) basis set (Rassolov et al., 2001). Upon completion of the energy minimizations, frequency calculations were conducted (with no imaginary frequencies in the final geometries). The model harmonic frequencies were scaled by 0.961 before comparing with observation to account for anharmonicity, basis set effects, and approximations in electron correlation. (Note that this is an approximate scaling factor based on the Scott and Radom value for B3LYP/6-31G(d) of 0.9614 (Scott and L, 1996).) To determine if there was a significant difference in the geometry or analytical frequencies, one cluster was optimized with and without implicit solvation, using a polarized continuum model (IEFPCM (Cancès et al., 1997) Solvent=Water). No significant differences were found in the geometry of the bound oxalate; however, there were differences in the frequencies (Table EA1). As the correlation of the theoretical frequencies to experiment was slightly worse when the PCM method was employed, and the computational time was markedly increased, the PCM method was not used (exceptions noted). As a check, one of the complexes was optimized employing the PCM=(water), but no significant changes were observed in either the geometry or energies of the frequencies. Vibrations were visualized with Chemcraft (<https://www.chemcraftprog.com>) and figures of complexes were made with VMD (Humphrey et al., 1996).

3. RESULTS

3.1. Characterization and properties of lepidocrocite samples

Transmission electron microscopy (TEM) images of the two lepidocrocite samples are shown in Figure 1. Lp-1 consisted of hedge-hog shaped spherical agglomerations (200-400 nm in diameter) of lath-like, very thin irregularly shaped sheets of 20-100 nm length width and less than 20 nm thickness (Figure 1A). The predominating surfaces of ideally crystallized sheets are the (010) surfaces. Lp-2 consisted of plate-like (50-100 nm width and 200-500 nm width) agglomerations of 200-500 long rods of 10 nm width and less than 10 nm thickness (Figure 1B). The predominating surfaces are (010) and (100), with lower contributions of (001) (Figure 1C) and other surfaces (not shown). The ideally crystallized (010) surface contains only “proton and ion-exchange inactive,” doubly coordinated surface hydroxyl groups ($\equiv\text{Fe}_2\text{-OH}$; $\mu\text{-OH}$ sites) that would not be expected to exchange with oxalate. The (100) surfaces contain two rows of “active” singly coordinated -OH groups ($\equiv\text{Fe-OH}$ sites) and on row of “inactive”, triply coordinated ($\equiv\text{Fe}_3\text{-OH}$; $\mu_2\text{-OH}$ sites). The (001) surface contains an equal numbers of singly and doubly coordinated hydroxyl groups. With ideal surfaces, we would expect a higher density of adsorption active sites on the rod-shaped Lp-2 (compared to the lath-shaped Lp-1 with mostly inactive 010 surfaces), despite of its lower specific surface area, and possibly observable differences in the spectra of oxalate adsorbed to the different samples. However, the 010 faces of lepidocrocite typically contain a large number of defect sites with also “active” singly coordinated -OH groups. It is suspected that the amount of defect sites associated with (010) surfaces of Lp-1 and -2 will lead to similar reactivities. For example, it was found that differences in lepidocrocite particle morphology or roughness did not significantly impact surface charge development (Hiemstra and van Riemsdijk, 2007).

3.2. ATR-FTIR spectra of oxalate in aqueous solution and adsorbed to lepidocrocite

The spectra of oxalate show distinct changes upon protonation and complexation to metal ions. The dissolved oxalate dianion with staggered D_{2d} or planar D_{2h} geometry has four equivalent C-O bonds and exhibits two strong infrared peaks in the range from 1300-1600 cm^{-1} . The symmetry is lowered with protonation and complexation, and new bands with predominantly $\nu(\text{C=O})$ character at high energy and mainly $\nu(\text{C-O})$ character at lower energy appear. In solution or surface complexes with BM structures in which oxalate has a close to C_{2v} symmetry, peaks in the 1690–1715 cm^{-1} and 1660–1690 cm^{-1} ranges, were assigned to symmetric $\nu_s(\text{C=O})$ and asymmetric $\nu_{as}(\text{C=O})$ coupled vibrations, and two strong peaks at 1390–1430 cm^{-1} and 1270–1320 cm^{-1} to $\nu_s(\text{C-O})+\nu(\text{C-C})$ and to $\nu_{as}(\text{C-O})$ stretching vibrations (Bhandari et al., 2010). Oxalate surface complexes as modeled here with complex clusters including surrounding water molecules, can deviate from C_{2v} symmetry and the assignment of vibrations might thus change.

3.2.1. Spectra of aqueous oxalate species

Figure 2A shows the pH-dependent spectra of oxalate in aqueous solution. Oxalic acid has a $\text{p}K_{a1}$ of 0.97 – 1.26 and a $\text{p}K_{a2}$ of 3.57 – 4.27, depending on the ionic strength (Axe and Persson, 2001; Yoon et al., 2004). In the IR spectrum of oxalic acid at pH 1.36, both the neutral and anionic species are seen in solution. As the pH is increased, the dianionic species becomes dominant; by pH 5.40 only the dianionic species, $\text{C}_2\text{O}_4^{2-}$, is seen. In the IR spectra of the dianion, two asymmetric $[\nu_a(\text{C-O})]$ stretches are seen at 1308 cm^{-1} and 1566 cm^{-1} , respectively. Using Raman spectroscopy, an additional symmetric $[\nu_s(\text{C-O}) \text{ p } (\text{C-C})]$ stretch is seen at 1456 cm^{-1} (Begun and Fletcher, 1963; Hind et al., 1998).

3.2.2. Spectra of oxalate adsorbed to Lp-1 and Lp-2 as a function of time and pH

Figures 2B and 2C show the spectra of adsorbed oxalate on Lp-1 and Lp-2, respectively, at different pH-values. The pH-values were decreased in rapid steps by addition of dilute HCl. Shown, are the spectra collected 30-40 min after each pH change, at which time the spectral amplitudes did not change by more than 1-2% in one minute. The amplitudes of several characteristic peaks as a function of time for Lp-2 are shown in Figure 2D. As the pH is lowered, increasing absorbances in the three ranges from (1) 1250 – 1320 cm^{-1} , (2) 1380-1470 cm^{-1} , and (3) 1560-1720 cm^{-1} are observed. Vibrations in the first two ranges are assigned to C-O stretches, while vibrations in the latter region are likely C=O stretches.

The peak-positions of adsorbed oxalate and the spectral changes with pH on Lp-1 and on Lp-2 are almost identical. Also observed on both samples, is the larger increase of the 1710-1711 cm^{-1} peak relative to the 1624-1625 cm^{-1} peaks when lowering the pH. The spectra of adsorbed oxalate measured on Lp-2 shows slightly more distinct features than on Lp-1. For example, the peaks at 1624, 1565, 1436, and 1309 cm^{-1} are more defined for Lp-2 than the corresponding shoulders at closely the same positions for Lp-1. The largest difference of the spectra on Lp-2 compared to Lp-1 is the higher amplitude of the two peaks at 1565 and 1309 cm^{-1} , which correspond closely to the peaks of aqueous oxalate. For a comparison, Figure EA1E shows additional spectra of oxalate on Lp-1 which were recorded with a slow adjustment of the pH to pre-set values by computer-controlled titrators (adapted, with data from (Hug and Bahnmann, 2006)). Due to slow pH-adjustment, these spectra were equilibrated for longer times and did not change more than 1% on a time scale of 10-20 minutes. The three data sets show the same spectral changes with pH: The peak positions and spectral changes for Lp-1 and Lp-2 were very similar and are clearly more complex than a simple increase of all peak amplitudes with decreasing pH. Most notably, the absorbance at 1710-1711 cm^{-1} shows the largest increase upon lowering the pH, while the absorbance increases less at 1685 and 1575 cm^{-1} and slightly decreases at 1565 cm^{-1} from pH 4.0 to 3.0. The plot of peak amplitudes against time (Figure 2D) also shows different kinetics at different wavelengths. For example, the amplitudes at 1309 cm^{-1} and 1565 cm^{-1} reach an equilibrium value at pH 6 much faster than the amplitudes at other peak positions. The different responses in time and with pH at different wavelengths are a clear indication that several surface complexes form at different rates, and that their relative contributions are pH-dependent.

3.2.3. Spectrum of oxalate on Lp-2 in D₂O

To explore the role of hydrogen bonding, the adsorption experiment was also conducted in D₂O (Figure 2E). In D₂O, all bands were still quite broad, with only small differences in peak positions and with the same spectral changes upon lowering the pD. Three defined peaks were evident at 1707, 1681, and 1631 cm^{-1} and were slightly more distinct than in H₂O. The broadness of the low-energy shoulder is reduced compared to the spectra on Lp-1 in Figure 2B, but the positions of all well-defined peaks are very similar and do not deviate by more than 5 cm^{-1} . That there are only minor changes between the spectra in H₂O and D₂O suggest that the main features of spectra of surface complexes of oxalate on lepidocrocite are not strongly affected by hydrogen bonding.

3.2.4. Spectra of dissolved Fe-oxalate complexes in H₂O and D₂O

The spectra of dissolved FeOx⁺ (Figure 2F) in H₂O and D₂O show peaks at 1712, 1691, 1390 and 1250 cm^{-1} , similar to the positions of adsorbed oxalate, but the broad absorbances between 1565-1680 cm^{-1} and 1400-1450 cm^{-1} of adsorbed oxalate are largely absent. If the spectrum of adsorbed oxalate with a BM structure is expected to be similar to that of dissolved FeOx⁺, then the additional features visible in Figures 2B-E would indicate the presence of additional surface complexes with different structures. The spectra of Fe(Ox)₂⁻ and Fe(Ox)₃³⁻ are similar, but the peak position at 1691 cm^{-1} in FeOx⁺ shifts to 1679 cm^{-1} and the amplitude increases. Since Fe(Ox)₂⁻ and Fe(Ox)₃³⁻ structures are not possible on the surface, the relevant comparison is the FeOx⁺ aqueous complex with similar amplitudes for the 1712 and 1691 cm^{-1} bands. This strengthens the evidence for an additional species with a different structure in the spectra of adsorbed oxalate.

3.3. Reactivity of adsorbed oxalate

3.3.1. Oxalate promoted dissolution rates and adsorption pH-edge

The surface concentration of oxalate on **Lp-2** and the reactivity of adsorbed oxalate on ligand controlled dissolution (total oxalate concentration = 500 μM) are shown in Figure 3. The rate coefficients of ligand controlled dissolution k_L have been calculated by rearrangement of the rate law for ligand controlled dissolution with $k_L = R_L / [L]_{\text{ads}}$, where R_L is the dissolution rate coefficient and $[L]_{\text{ads}}$ is the surface loading of oxalate. The corresponding data of Fe vs. time is shown in Figure EA2. Decreasing dissolution rate coefficients with increasing pH are indicative of changes in the surface speciation of the adsorbed ligand with a decreasing proportion of such species that serve as precursors of the rate-determining dissolution step. As will be shown in the discussion section, this observation is consistent with decreasing proportions of BM surface complexes and a shift towards less reactive MM and OS complexes with increasing pH.

3.3.2. Photochemical reactivity

In addition to differences of dissolution rates induced by different surface complexes, we expect different photochemical reactivities. Spectra collected during the adsorption of oxalate to **Lp-1** (Figure 4A) and the effects of subsequent illumination with 365 nm light are shown in Figure 4 B-D. During each of two illumination periods of 180 s, a fast temporary decrease of the oxalate absorbance is observed. The response is proportionally most pronounced at 1708 cm^{-1} (39% decrease) to a lesser degree 1679 cm^{-1} (17% decrease) and much less at 1435, 1409, 1308 and 1276 cm^{-1} (less than 12% decrease). The difference spectra shown in Figure 4C and the corresponding amplitude changes in Figure 4D shows that the spectral features that decrease most strongly during irradiation resemble predominantly a spectrum similar to dissolved FeOx^+ .

4. DISCUSSION

The experimental results show that oxalate forms several surface complexes on the surface of lepidocrocite, with different adsorption kinetics and contributions depending on pH. Dissolution and photochemical experiments additionally provide evidence for the presence of several surface complexes with different reactivities. In order to compare experimental and calculated spectra, a separation of the experimentally measured spectra into contributions of different surface complexes is required. In the following, we describe the separation of spectra and the assignment of structures by comparison of measured frequencies with the calculated frequencies for a range of possible structures.

4.1. Separation of spectra from different surface complexes

The minimum number of spectra needed for each data set was determined by Singular Value Decomposition (SVD). As shown in the Supporting information (SI) in Figures EA3 and EA4, the data sets with oxalate adsorbed on **Lp-1** and **Lp-2** could be reproduced within signal-noise by a linear combination of 3-5 SVD-components. Three components provided an adequate fit, with only small improvements with 4 and 5 components. We thus work on the basis that three surface complexes with distinct spectra can provide a satisfactory explanation for our experimental observations. Since we have no model describing the quantitative contribution of each spectrum as a function of pH and time that would allow us to transform the orthogonal SVD components (with both positive and negative amplitudes) into physically meaningful spectra of surface complexes, further assumptions have to be made. Spectra of surface complexes can only have positive amplitudes and should consist of a sum of line shapes from individual vibrations, with frequencies that can be compared to calculated frequencies. As the peaks in our spectra are rather broad due to Doppler and proximity broadening they are best described by Gaussian (rather than by Lorentzian) line shapes.

We thus searched for spectra of three different surface complexes consisting of Gaussian line shapes, guided by the observations of the measured spectra and the results from DFT calculations (explained in detail in the next section). The data in [Figures 2B-E](#) show spectral features (peaks at 1308-1311 cm⁻¹ and 1565-1567 cm⁻¹) that closely resemble the spectrum of aqueous C₂O₄²⁻, particularly at pH 5-7 and at early times. Based on the DFT calculations, we expect two peaks for dissolved oxalate and for outer-sphere adsorbed oxalate. Upon lowering of the pH to 4.5, we observe increasing spectral contributions in the three ranges from 1250-1320 cm⁻¹, 1380-1470 cm⁻¹ and 1560-1720 cm⁻¹, with relatively small contributions at 1700-1720 cm⁻¹. From pH 4.5-3.0, all contributions except those resembling the aqueous C₂O₄²⁻ dianion further increase, but the increase is disproportionally stronger for the relatively sharp peak at 1707-1711 cm⁻¹. These observations suggest the formation of an OS complex at early times and higher pH, and the formation of two inner-sphere complexes at lower pH. Based on interpretations of previous studies, the two consistently most prominent peaks at low pH at 1707-1711 cm⁻¹ and 1681-1685 cm⁻¹ and the peaks at 1404-1410 cm⁻¹ and 1273-1275 cm⁻¹ are due to the spectrum of BM or BB surface complex ([Axe and Persson, 2001](#); [Bhandari et al., 2010](#); [Duckworth and Martin, 2001](#); [Hug and Bahnemann, 2006](#); [Hug and Sulzberger, 1994](#); [Yoon et al., 2004](#)). The calculations predict 5 observable peaks for a BM or a BB complex. The spectral contributions that are the most prominent at early times at pH 6 at 1674-1676 cm⁻¹, 1428-35 cm⁻¹ and around 1250-80 cm⁻¹ are due to a third, not yet assigned, spectrum. The calculations suggest the possible formation of a MM complex with 4 peaks in this region and a fifth peak overlapping with the peak of the BB complex. Based on the calculations, we thus expect that 5+4+2=11 peaks with Gaussian line shapes should be able to adequately explain the spectra.

To test whether 11 Gaussians are sufficient, and to obtain preliminary information about possible peak locations, each measured spectrum was individually fit with 11 Gaussians, as shown in [Figure EA5](#) for the spectrum of oxalate adsorbed to **Lp-1** at pH 4.0. Guided by the calculated spectra (discussed later), the Gaussians were tentatively grouped as belonging to a BM (red lines with 5 Gaussians), MM (blue lines with four Gaussians) and OS (green lines with two Gaussians). All other measured spectra could similarly be fit to within-signal-to-noise, with 11 Gaussians. The resulting peak positions are listed in [Table EA2](#). Some vibrations shift slightly with pH changes (by an average of ±2 cm⁻¹), but the same number of Gaussian line shapes with similar peak maxima can explain all spectra. However, fits with 11 Gaussians for each measured spectrum separately allowed a change of relative amplitudes and peak-widths and do not yet provide three consistent spectra with fixed peak positions, widths and amplitudes. Consistent spectra for three surface complexes were found by linear combination fitting as described in the following.

4.1.1. Fits of data sets with three spectra consisting of fixed Gaussian line shapes

As explained above, assuming that each spectrum of three formed surface complexes (S_{OS}, S_{MM} and S_{BM}) does not change strongly with pH or surface concentration, linear combinations of these spectra (here arranged as columns in matrix **S**) should be able to reproduce the measured data-sets (arranged as columns in matrix **M**) in linear combinations as described by matrix **C**:

$$\mathbf{M} = \mathbf{S} \cdot \mathbf{C} \quad (1)$$

with the three spectra in **S** described by a sum Gaussian lineshapes (G):

$$\begin{aligned} S_{OS} &= G_{11}(v_{11}, w_{11}, a_{11}=1) + G_{12}(v_{12}, w_{12}, a_{12}) \\ S_{MM} &= G_{21}(v_{21}, w_{21}, a_{21}=1) + G_{22}(v_{22}, w_{22}, a_{22}) + G_{23}(v_{23}, w_{23}, a_{23}) + G_{24}(v_{24}, w_{24}, a_{24}) \\ S_{BM} &= G_{31}(v_{31}, w_{31}, a_{31}=1) + G_{32}(v_{32}, w_{32}, a_{32}) + G_{33}(v_{32}, w_{32}, a_{32}) + G_{34}(v_{32}, w_{32}, a_{32}) + G_{35}(v_{35}, w_{35}, a_{35}) \end{aligned} \quad (2)$$

Where $G_{ij}(v_{ij}, w_{ij}, a_{ij}) = a_{ij} \cdot \exp(-(v - v_{ij}) / (1.4142 \cdot w_{ij} / 2.3548))^2)$

a_{ij} are the amplitudes, v_{ij} the positions of the peak maxima and w_{ij} the peak widths at half maximum.

The first amplitude (peak at the lowest wavelength) of each spectrum was fixed to 1.0. Fixing one

amplitude for each spectrum is necessary to obtain fixed spectra for each surface complex, as their overall amplitudes (contributions) to the measured spectra are optimized with matrix **C**, computed with Matlab from the pseudo-inverse of **S**:

$$\mathbf{C} = \text{pinv}(\mathbf{S}) * \mathbf{M} \quad (3)$$

All other 30 parameters (8 amplitudes, 11 peak position and 11 widths) were adjustable. As initial parameters for the peak maxima and widths, we used the average of the parameters obtained from the Gaussian fits to the individual spectra, as listed in Table EA2. The parameters for the three fixed spectra were optimized with the Nelder-Simplex routine in Matlab, by minimizing the sum of squared differences (SSr) between the measured and the reproduce spectra:

$$\text{SSr} = \sum_i \sum_j (\mathbf{M} - \mathbf{S} * \mathbf{C})^2 \quad (4)$$

The results of a fit to the combined kinetics and pH-dependence on **Lp-2** are shown in Figure 5 A1-A3. A1 shows the measured spectra, A2 the reproduced spectra offset by 0.03 units, and A3 the residuals (measured- reproduced spectra) offset by 0.6 units. The fit is not perfect (as expected), but the reproduced spectra capture the main features and changes of the measured spectra. The resulting separated spectra are shown in Figure 5B. The spectrum S_{OS} closely resembles the spectrum of the dissolved oxalate dianion (Figure 2A) and S_{BM} resembles the spectrum of the dissolved FeOx^+ complex (Figure 2F), while S_{MM} does not show similarity to any of the dissolved spectra. Figure 5C shows the contributions of the three spectra as a function of time and pH. The spectrum S_{OS} saturates quickly upon addition of oxalate at pH 5.9, but its contribution decreases within the next 40 minutes in favor of S_{MM} and S_{BM} . Upon lowering the pH to 3.0, the relative contributions of S_{BM} increase while the relative contributions of S_{MM} and particularly of S_{OS} decrease. The results of fits to other data sets and the ranges and standard deviations for peak positions are shown in Figures EA6 and EA7 and listed in Table EA3. The shape of separated spectra and the peak positions show some variation, but the main characteristics of the separated spectra are consistent and the peak position of the main peaks agree to $\pm 2 \text{ cm}^{-1}$ for the 1708-1711 cm^{-1} to $\pm 8 \text{ cm}^{-1}$ for most other peaks. The most unreliable peak positions are the ones of BM complex around 1643 (± 28) cm^{-1} and of the MM complex around 1611 (± 18) cm^{-1} . This is due to overlap of BM and MM peaks in this spectral regions and to lower signal-to-noise and background subtraction of the strong water peak of the electrolyte around 1630 cm^{-1} . Despite the uncertainties, the separated spectra for BM complex consistently resembles the aqueous FeOx^+ complex and the spectra of the OS agrees very well with the spectrum of aqueous oxalate. The spectrum of the MM complex does not resemble any of the reference spectra, but its formation and the infrared frequencies in this range are predicted by the calculations. The mean values used for comparison with calculated frequencies and the standard deviations are listed in Table 1.

4.2. DFT-calculations and identification of the structure of adsorbed complexes

The adsorption of oxalate to two surfaces of lepidocrocite, (100) and (010), representing surfaces with either terminal or shared OH groups, were modeled, as shown in Figure 6. For the (100) surface, possible adsorption structures fall into four main categories: 1) the oxalate is bonded to a single Fe atom through one O atom, *monodentate mononuclear* (MM), 2) the oxalate is bonded to a single iron atom through two O atoms, *bidentate mononuclear*, either with two O atoms from the same carboxylic group (BM') or with one O atom of each carboxylic group (BM), 3) the oxalate is bonded to two Fe atoms through two O atoms, *bidentate binuclear*, again with O atoms from the same (BB') or from both carboxylic groups (BB and BB*). Because the hydroxyl groups on the (010) surface are shared between two Fe atoms, bonding structures had to be slightly modified; the MM became a *monodentate binuclear* (MB), the BB' a BTetra₁, and the BB became either a *bidentate tetranuclear* (BTetra₂) or a *bidentate trinuclear* (BTri) structure. 4) Instead of replacing surface hydroxyl groups

and forming direct bonds to surface Fe atoms, the oxalate could be hydrogen-bonded to hydroxyl groups attached to the Fe atoms, *hydrogen-bonded outer sphere (HOS)*. This is not shown here, but discussed later.

4.2.1. Calculation of adsorption energies with periodic structures (VASP)

Calculations of the periodic cells were first carried out on energy-minimized structures of the periodic cells representing a “dry” surface. The energies of these models were used to determine the relative stability of various bonding configurations of oxalate (Table 2). The most stable configurations on the “dry” surfaces were found to be **BTri** on the (010) and **BM** on the (100) surface. More realistic adsorption energies (ΔE_{ads}) for aqueous systems were then calculated for “solvated” surfaces, as shown for **OS**, **BM** and **MM** in Figure 7. The ΔE_{ads} of **BM** and **MM** on the (100) surface (Figure 7) were found to be -89 and -98 kJmol⁻¹, respectively, whereas the ΔE_{ads} of **BTri** on the (010) surface (structure not shown) was found to be +29 kJmol⁻¹. The negative values favor adsorption and are similar to other calculated ΔE_{ads} of small organic and inorganic molecules to iron(hydr)oxide and other mineral surfaces (Gusain et al., 2016; Hansmann and Anderson, 1985; Kubicki, 2006; Kubicki et al., 2012; Mendive et al., 2009; Otte et al., 2013).

4.2.2. Calculation of vibrational frequencies in representative molecular clusters (Gaussian)

Calculating the vibrational frequencies of the periodic cells is computationally demanding and the numerical frequencies are not as accurate as analytical frequencies. Furthermore, IR intensities were not available through the periodic VASP calculations. Therefore, vibrational calculations were performed with molecular clusters extracted from the energy-minimized 100 and 010 surfaces.

Validation of theoretical frequencies with dissolved oxalate species. To validate our methods, oxalic acid, the oxalate dianion, and trioxalatoiron(III) (Figure EA8) were energy-minimized and the analytical frequencies were obtained (B3LYP/6-31G(d,p)/PCM(water)) (Akutsu et al., 2004; Begun and Fletcher, 1963; Domagal-Goldman and Kubicki, 2008; Fujita et al., 1962a, b; Gouteron, 1976; Hind et al., 1998; Homborg and Preetz, 1976; Martin and Pinkerton, 1998; Öhrström and Michaud-Soret, 1999; Persson and Axe, 2005; Shippey, 1980). The optimized structure of oxalic acid and trioxalatoiron(III) were compared to crystal structure data and found to be in excellent agreement (except for the FeO-C bond), suggesting that the intramolecular forces are being properly accounted for (Table EA4). A comparison involving oxalate was omitted; although the crystal structure is D_{2h} symmetry, in aqueous solution the dianion adopts a symmetry closer to D_{2d} . (Hind et al., 1998) Based on slope, R^2 , y-intercept, and standard deviation of error (Figure EA9, Table EA5), the calculated frequencies correlated well with observation (Table EA5). Trioxalatoiron(III) had an excellent correlation, whereas the correlation (R^2) and the slope and intercept for oxalic acid was less accurate. It is hypothesized that hydrogen-bonding stabilization of the acid to the aqueous solution is not being fully accounted for in the model. For the oxalate dianion, the complex receives greater stability from hydrogen-bonding to the aqueous solution, so the deficiency in the model is more pronounced, yielding a slope and intercept that deviates more from 1.0 and 0, respectively, than that for the parent acid. This suggests that error is expected for the calculated OS complex frequencies, the calculated frequencies for the covalently bonded inner-sphere complexes are expected to have smaller errors.

4.2.3. Structural assignments of surface complexes by comparison of experimental and calculated vibrational frequencies

Molecular clusters corresponding to the geometries in Figure 6 are shown in Figure 8, with oxalate bound to clusters of eight Fe atoms representing the (100) and (010) lepidocrocite surfaces, including coordinated H₂O/OH. Seven additional structures were evaluated, shown in Figure EA10. All structures were energy-minimized, with the analytical frequencies subsequently determined (B3LYP/6-31G(d,p)). With regards to the bonded oxalate, there were minimal geometry changes between the molecular clusters compared to the periodic cells (Table EA6). The analytical frequencies from the molecular cluster with adsorbed oxalate were subtracted from those of the

corresponding solvated molecular clusters without oxalate (Figure EA11) to subtract the vibrations of coordinated water. Of the remaining frequencies, only those dominated by an oxalate vibration were considered.

In order to compare calculated analytical frequencies to experiment, the average Gaussian peak positions obtained by Gaussian fitting of the experimental spectra were employed. The theoretical frequencies were then correlated to Gaussian peaks of either S_{BM} or S_{MM} by linear regression (Figure EA12 and Table EA7). Good agreement between experimental and calculated frequencies was indicated by a slope close to 1.0 and an intercept close to 0. We rejected all structures that lead to slopes <0.95 and >1.05 and with intercepts deviating from zero by more than 70 cm^{-1} . Structures for which an experimentally observed frequency was not predicted by the calculation were also rejected. An additional measure was the average (absolute) difference between experimental and calculated frequencies.

The bonding geometries **BM'**, **BB'**, **BB**, **BB***, **MB**, **BTetra₁**, **BTetra₂**, shown in Figure EA10, all had poor correlation or missing frequencies (Figure EA12 and Table EA7) and were not considered further. There was an acceptable correlation for **MB**, but the experimental frequency at $1664 \pm 9\text{ cm}^{-1}$ was not reproduced theoretically, so this configuration was also discounted. Much better correlations and no missing frequencies were obtained for the bonding geometries **MM**, **BM** and **BTri** shown in Figure 8. The linear regression fits for these structures are shown in Figure 9 and the corresponding parameters in Table 1a. Among these structures, **BM** and **MM** had the lowest average differences of all considered structures and are thus the most likely structures formed in agreement with the observed spectra. Surprisingly, between **BM** and **MM**, there is no significant difference to the oxalate in geometry, bond order, or Mulliken charges (Tables EA8a,b).

A bonding structure similar to **BM** was proposed for oxalate adsorbed to ferrihydrite (pH = 4.5), goethite (pH = 3.13 – 7.87), hematite (pH = 5.0), boehmite (pH = 5.1), corundum (pH = 5.1). (Axe et al., 2006; Bhandari et al., 2010; Duckworth and Martin, 2001; Yoon et al., 2004). Hug and Sulzberger (Hug and Sulzberger, 1994) had previously postulated the involvement of a protonated BM and/or BB structure at low pH on TiO_2 , but were unable to explore the idea further. To address this, one of the non-coordinated oxalic O of the **BM** cluster was protonated (Figure EA13). The experimental frequencies at 1403 cm^{-1} and 1684 cm^{-1} were modeled well, but the frequencies at 1275 cm^{-1} and 1712 cm^{-1} were not (average difference from experiment was 23 cm^{-1}), and the frequency at 1641 cm^{-1} was not predicted (Table EA9). It is therefore unlikely that a protonated oxalate is adsorbed to the lepidocrocite surface. Axe (Axe et al., 2006) and Bahndari (Bhandari et al., 2010) had previously suggested that in addition to inner-sphere adsorption, hydrogen-bonded outer-sphere complexes could also be formed. To explore this, two HOS clusters were built, one modeling the (010) surface (**HOS₍₀₁₀₎**) and one modeling the (100) surface (**HOS₍₁₀₀₎**) (Figure EA14). Four and five frequencies were predicted for **HOS₍₀₁₀₎** and **HOS₍₁₀₀₎**, respectively, suggesting that our S_{OS} spectra with only two frequencies arises from a true outer-sphere complex, rather than a hydrogen-bonded complex. For **HOS₍₀₁₀₎**, the theoretical frequencies correlated well with the S_{MM} Gaussian peaks (Figure EA15), but for both complexes, the observed frequency at 1664 cm^{-1} is not reproduced (Table 1). This suggests that while S_{MM} arises from **MM**, **HOS₍₀₁₀₎** could also be present. The correlation of **HOS₍₁₀₀₎** to S_{MM} is rather poor, suggesting that for the (100) surface, once the oxalate is close enough to directly hydrogen bond to the surface, an inner-sphere complex is immediately formed. The presence of a significant fraction of **HOS** would be expected to lead to large shifts in peak maxima when H_2O is replaced with D_2O , while we observed only peak shift in the order of $3\text{--}5\text{ cm}^{-1}$ (Figures 2c and 2e). Thus, both experiments and calculations provide no evidence for a detectable contribution of HOS from pH 4-7.

4.3. Structure and reactivity of different surface complexes

4.3.1. Oxalate adsorption pH-edge and ligand promoted dissolution rates

In the ligand promoted dissolution by oxalate, it is generally assumed that BM complexes have a stronger effect on the kinetic labilization of surface sites. This is consistent with our spectral and

structural analysis, indicating a decreasing proportion of **BM** surface complexes and a shift towards less reactive **MM** and **OS** complexes with increasing pH. In Figure 3, the pH-dependence of the surface concentration of adsorbed oxalate measured in batch experiments is closely matched by the sum of complexes measured by FTIR, while the dissolution rates are matched by the separated spectral contribution of the BM surface complex. This observation confirms that the dissolution rate is not proportional to the sum of adsorbed complexes, but to the concentration of the most reactive surface complex (Banwart et al., 1989).

4.3.2. Photochemical reactivity

Dissolved Fe-oxalate complexes are coordinated in a **BM** structure and show high photo-reactivity, with quantum yields of 0.6-1.0 for the formation of Fe(II) upon irradiation with UV-light (Faust and Zepp, 1993). We could expect similarly high photo-reactivities for **BM** surface complexes, whereas the photo-reactivities are expected to be lower for BB and MM structures and absent for OS complexes. This is confirmed by our experimental observation in that the spectrum of the rapidly photolyzed complex is most similar to the spectrum of **BM**. The same spectral features also increase most strongly again after the irradiation stops (Figure 4C). We interpret this as clear evidence for a higher photo-reactivity of the surface complex assigned with a **BM** structure. During the UV-irradiation, the BM complex is photolyzed more quickly than it can reform by equilibration with the less active surface complexes and the oxalate in solution. The equilibrium is re-established after the illumination stops. Interestingly, the spectrum of OS also decreases during irradiation, which could be due to electrostatic repulsion of oxalate dianions from the surface by the photochemical formation of CO_2^- .

5. CONCLUSIONS AND IMPLICATIONS

The combined results of this study show that the formation of several surface complexes of oxalate with different structures is supported both by FTIR-measurements and by DFT-calculations, with good agreement between experimental and calculated frequencies for BM, MM and OS structures. As shown here, the reactivities of these complexes are different and need to be considered in order to understand surface reactions, such as mineral dissolution and photochemical reactions. Isotherms derived from measurements of the overall adsorption of oxalate quantify the surface concentration of adsorbed oxalate, but do not provide information about the speciation and structure of adsorbed oxalate which determine its reactivity. The number of different complexes and their possible structures can be assessed with a combination of experimental and theoretical methods. A series of spectroscopic measurements performed as a function of several variables, such as pH and time is necessary for a separation of spectra of several surface complexes.

Theoretical calculations with clusters representative of surface sites, performed at the level presented in this study are sufficiently precise to guide the interpretation of the spectra and to identify the major structures that agree best with measured frequencies. However, the correlations between measured frequencies and calculations are often close for several structures. It can thus be difficult to decide whether the different structures exist, or if differences between theory and experiments are sufficient to rule out certain structures. It can also not be ruled out that ranges of different structures are formed and that their spectra exhibit continuous shifts in peak positions as a response to changes in concentration and pH. Even if this is the case, it should still be possible to find a smaller number of spectra and structures that are representative of possible substructures (e.g. structures with different coordinations of water). The limitation to Gaussian line shapes is most likely the main reason for the less than perfect agreement of our fits with the measured spectra. The spectral features between $1600\text{-}1650\text{ cm}^{-1}$ are uncertain due to the difficult subtraction of vibrational bands of water associated with the surface or with surface complexes and should be interpreted with care. Nevertheless, all the experimentally observed important changes in the spectra are reproduced well. In combination with the DFT calculations, it was possible to narrow the important structures of

surface complexes down to **OS**, an **MM** and a **BM**.

The proposed structures and spectra can rationalize several independent experimental observations. 1) They explain the observed IR-spectra as a function of time and pH. 2) They explain how ligand-promoted dissolution rates of lepidocrocite with oxalate are not proportional to the total surface concentrations of adsorbed oxalate, but show a much steeper decrease with increasing pH, which is consistent with the expectation that surface complexes with **BM** structures are the most active in promoting dissolution. 3) The expected reactivities of the proposed structures agree with photochemical experiments, which show that the spectral contributions assigned to the **BM** complex disappears at the fastest rate under UV-irradiation. The **BM** complex is expected to be similarly photo-reactive as the corresponding solution complex, which is photolyzed with a quantum yield around 0.5. In contrast, the **MM** complex is not expected to be nearly as photo-reactive, similarly to surface complexes of malonate and succinate (Borer et al. 2014). Although the IR-spectra with **Lp-2** are generally somewhat better defined than with **Lp-1**, the observed spectral differences are small. The difference of the fractions of dominant crystal faces in our two samples are either too small, or the crystal faces are not ideally crystallized and contain many defect sites that diminish the difference between the different surfaces. This indicates that the overall results and conclusions are likely valid for differently prepared synthetic lepidocrocite samples, and possibly also for naturally occurring lepidocrocite phases.

ACKNOWLEDGEMENTS

Thomas Ruttimann (Eawag, Switzerland) is acknowledged for assistance with laboratory experiments and ICP-MS analyses. This project was financially supported by the Swiss National Science Foundation under contracts Nos. 200021L_150150 "Synergistic effects of redox processes and ligand controlled dissolution of iron(hydr)oxide phases" Mathematics, Natural sciences and Engineering (division II).

APENDIX A. SUPPLEMENTARY DATA

Supplementary data associated with this article can be found in the online version.

REFERENCES

- Accelrys Software, I. (2007) Materials Studio. Accelrys Software, Inc., San Diego.
- Akutsu, H., Akutsu-Sato, A., Turner, S.S., Day, P., Canadell, E., Firth, S., Clark, R.J.H., Yamada, J.I. and Nakatsuji, S. (2004) Superstructures of donor packing arrangements in a series of molecular charge transfer salts. *Chem. Commun.* 10, 18-19.
- Axe, K. and Persson, P. (2001) Time-dependent surface speciation of oxalate at the water-boehmite (g-AlOOH) interface: Implications for dissolution. *Geochim. Cosmochim. Acta* 24, 4481-4492.
- Axe, K., Vejgård, M. and Persson, P. (2006) An ATR-FTIR spectroscopic study of the competitive adsorption between oxalate and malonate at the water-goethite interface. *J. Colloid Interface Sci.* 294, 31-37.
- Banwart, S., Davies, S. and Stumm, W. (1989) The role of oxalate in accelerating the reductive dissolution of hematite (α -Fe₂O₃) by ascorbate. *Colloids and Surfaces* 39, 303-309.
- Becke, A.D. (1993) Density-functional thermochemistry. III. The role of exact exchange. *J. Chem. Phys.* 98, 5648-5652.
- Begun, G.M. and Fletcher, W.H. (1963) Vibrational spectra of aqueous oxalate ion. *spectrochimica Acta* 19, 1343-1349.

- Bhandari, N., Hausner, D.B., Kubicki, J.D. and Strongin, D.R. (2010) Photodissolution of Ferrihydrite in the Presence of Oxalic Acid: An In Situ ATR-FTIR/DFT Study †. *Langmuir* 26, 16246-16253.
- Blöchl, P.E. (1994) Projector Augmented-Wave Method. *Phys. Rev. B: Condens. Matter Mater. Phys.* 50, 17953-17979.
- Borer, P. and Hug, S.J. (2014) Photo-redox reactions of dicarboxylates and α -hydroxydicarboxylates at the surface of Fe(III)(hydr)oxides followed with in situ ATR-FTIR spectroscopy. *J. Colloid Interface Sci.* 416, 44-53.
- Borer, P., Hug, S.J., Sulzberger, B., Kraemer, S.M. and Kretzschmar, R. (2007) Photolysis of citrate on the surface of lepidocrocite: An in situ attenuated total reflection infrared spectroscopy study. *J. Phys. Chem. C* 111, 10560-10569.
- Borer, P., Sulzberger, B., Hug, S.J., Kraemer, S.M. and Kretzschmar, R. (2009) Photoreductive dissolution of iron(III) (Hydr)oxides in the absence and presence of organic ligands: Experimental studies and kinetic modeling. *Environ. Sci. Technol.* 43, 1864-1870.
- Cancès, E., Mennucci, B. and Tomasi, J. (1997) A new integral equation formalism for the polarizable continuum model: Theoretical background and applications to isotropic and anisotropic dielectrics. *Journal of Chemical Physics* 107, 3032-3041.
- Cheah, S.F., Kraemer, S.M., Cervini-Silva, J. and Sposito, G. (2003) Steady-state dissolution kinetics of goethite in the presence of desferrioxamine B and oxalate ligands: Implications for the microbial acquisition of iron. *Chem. Geol.* 198, 63-75.
- Coey, J.M.D., Barry, A., Brotto, J.M., Rakptp, H., Brennan, S., Mussel, W.N., Collomb, A. and Fruchart, D. (1995) Spin Flip in Goethite. *J. Phys.* 7, 759-768.
- Cornell, R.M. and Schwertmann, U. (2003) *The Iron Oxides: Structure, Properties, Reactions, Occurrences, and Uses*, 2nd ed.; ed. Wiley-VCH, New York, NY, USA.
- Cwiertny, D.M., Hunter, G.J., Pettibone, J.M., Scherer, M.M. and Grassian, V.H. (2009) Surface chemistry and dissolution of α -FeOOH nanorods and microrods: Environmental implications of size-dependent interactions with oxalate. *J. Phys. Chem. C* 113, 2175-2186.
- Degenhardt, J. and McQuillan, A.J. (1999) Mechanism of oxalate ion adsorption on chromium oxide-hydroxide from pH dependence and time evolution of ATR-IR spectra. *Chem. Phys. Lett.* 311, 179-184.
- Deutsch, F., Hoffmann, P. and Ortner, H.M. (2001) Field experimental investigations on the Fe(II)- and Fe(III)-content in cloudwater samples. *J. Atmos. Chem.* 40, 87-105.
- Domagal-Goldman, S.D. and Kubicki, J.D. (2008) Density functional theory predictions of equilibrium isotope fractionation of iron due to redox changes and organic complexation. *Geochim. Cosmochim. Acta* 72, 5201-5216.
- Duckworth, O.W. and Martin, S. (2001) Surface complexation and dissolution of hematite by C1-C6 dicarboxylic acids at pH = 5.0. *Geochim. Cosmochim. Acta* 65, 4289-4301.
- Dudarev, S.L., Botton, G.A., Savrasov, S.Y., Humphreys, C.J. and Sutton, A.P. (1998) Electron-Energy-Loss Spectra and the Structural Stability of Nickel Oxide: An LSDA+U Study. *Phys. Rev. B: Condens. Matter Mater. Phys.* 57, 1505-1509.
- Faust, B.C. and Zepp, R.G. (1993) Photochemistry of aqueous iron(III)-polycarboxylate complexes: Roles in the chemistry of atmospheric and surface waters. *Environ. Sci. Technol.* 27, 2517-2522.
- Frisch, M.J., Trucks, G.W., Schlegel, H.B., Scuseria, G.E., Robb, M.A., Cheeseman, J.R., Scalmani, G., Barone, V., Mennucci, B., Petersson, G.A., Nakatsuji, H., Caricato, M., Li, X., Hratchian, H.P., Izmaylov, A.F., Bloino, J., Zheng, G., Sonnenberg, J.L., Hada, M., Ehara, M., Toyota, K., Fukuda, R., Hasegawa, J., Ishida, M., Nakajima, T., Honda, Y., Kitao, O., Nakai, H., Vreven, T., Montgomery, J.A., Jr., Peralta, J.E., Ogliaro, F., Bearpark, M., Heyd, J.J., Brothers, E., Kudin, K.N., Staroverov, V.N., Kobayashi, R., Normand, J., Raghavachari, K., Rendell, A., Burant, J.C., Iyengar, S.S., Tomasi, J., Cossi, M., Rega, N., Millam, J.M., Klene, M., Knox, J.E., Cross, J.B., Bakken, V., Adamo, C., Jaramillo, J., Gomperts, R., Stratmann, R.E., Yazyev, O., Austin, A.J., Cammi, R., Pomelli, C., Ochterski, J.W., Martin, R.L., Morokuma, K., Zakrzewski, V.G., Voth, G.A., Salvador, P., Dannenberg, J.J., Dapprich, S., Daniels, A.D., Farkas, Ö., Foresman, J.B., Ortiz, J.V., Cioslowski, J. and Fox, D.J. *Gaussian 09, Revision D.01*. Gaussian, Inc., Wallingford, CT.

- Fujita, J., Martell, A.E. and Nakamoto, K. (1962a) Infrared spectra of metal chelate compounds. VI. A normal coordinate treatment of oxalato metal complexes. *J. Chem. Phys.* 36, 324-331.
- Fujita, J., Martell, A.E. and Nakamoto, K. (1962b) Infrared spectra of metal chelate compounds. VII. Normal coordinate treatments on 1:2 and 1:3 oxalato complexes. *J. Chem. Phys.* 36, 331-338.
- Gouteron, J. (1976) Spectres de vibration de composés de coordination trichelates-I Composés trioxaliques. *Journal of Inorganic and Nuclear Chemistry* 38, 55-61.
- Gusain, D., Srivastava, V., Sillanpää, M. and Sharma, Y.C. (2016) Kinetics and isotherm study on adsorption of chromium on nano crystalline iron oxide/hydroxide: linear and nonlinear analysis of isotherm and kinetic parameters. *Res Chem Intermed* 42, 7133-7151.
- Hansmann, D.D. and Anderson, M.A. (1985) Using electrophoresis in modeling sulfate, selenite, and phosphate adsorption onto goethite. *Environ. Sci. Technol.* 19, 544-551.
- Hiemstra, T. and van Riemsdijk, W.H. (2007) Adsorption and surface oxidation of Fe(II) on metal (hydr)oxides. *Geochim. Cosmochim. Acta* 71, 5913-5933.
- Hind, A.R., Bhargava, S.K., Van Bronswijk, W., Grocott, S.C. and Eyer, S.L. (1998) On the Aqueous Vibrational Spectra of Alkali Metal Oxalates. *Applied Spectroscopy* 52, 683-691.
- Homborg, H. and Preetz, W. (1976) Tieftemperatur-Raman-Messungen an rotierenden festen Proben. *Spectrochim. Acta Part A Mol. Spectrosc.* 32, 709-716.
- Hug, S.J. and Bahnemann, D. (2006) Infrared spectra of oxalate, malonate and succinate adsorbed on the aqueous surface of rutile, anatase and lepidocrocite measured with in situ ATR-FTIR. *J Electron Spectrosc Relat Phenom* 150, 208-219.
- Hug, S.J. and Sulzberger, B. (1994) In situ Fourier transform infrared spectroscopic evidence for the formation of several different surface complexes of oxalate on TiO₂ in the aqueous phase. *Langmuir* 10, 3587-3597.
- Humphrey, W., Dalke, A. and Schulten, K. (1996) VMD: visual molecular dynamics. *J. Mol. Graphics Modell.* 14, 33-38.
- Kraemer, S.M. (2004) Iron oxide dissolution and solubility in the presence of siderophores. *Aquatic Sci.* 66, 3-18.
- Kresse, G. and Furthmüller, J. (1996) Efficient Iterative Schemes for Ab Initio Total-Energy Calculations Using a Plane-Wave Basis Set. *Phys. Rev. B: Condens. Matter Mater. Phys.* 54, 11169-11186.
- Kresse, G. and Joubert, D. (1999) From Ultrasoft Pseudopotentials to the Projector Augmented-Wave Method. *Phys. Rev. B: Condens. Matter Mater. Phys.* 59, 1758-1775.
- Kubicki, J.D. (2006) Comparison of As(III) and As(V) complexation onto Al- And Fe-hydroxides, in: O'Day, P.A., Vlassopoulos, D., Meng, X., Benning, L.G. (Eds.), *ACS Symposium Series*, 915, pp. 104-117.
- Kubicki, J.D., Paul, K.W., Kabalan, L., Zhu, Q., Mrozik, M.K., Aryanpour, M., Pierre-Louis, A.M. and Strongin, D.R. (2012) ATR-FTIR and density functional theory study of the structures, energetics, and vibrational spectra of phosphate adsorbed onto goethite. *Langmuir* 28, 14573-14587.
- Kubicki, J.D., Paul, K.W. and Sparks, D.L. (2008) Periodic density functional theory calculations of bulk and the (010) surface of goethite. *Geochemical Transactions* 9, 4.
- Laasonen, K., Car, R., Lee, C. and Vanderbilt, D. (1991) Implementation of Ultrasoft Pseudopotentials in Ab Initio Molecular Dynamics. *Phys. Rev. B: Condens. Matter Mater. Phys.* 43, 6796-6799.
- Lee, C., Yang, W. and Parr, R.G. (1988) Development of the Colle-Salvetti correlation-energy formula into a functional of the electron density. *Phys. Rev. B* 37, 785-789.
- Loring, J.S., Simanova, A.A. and Persson, P. (2008) Highly mobile iron pool from a dissolution-readsorption process. *Langmuir* 24, 7054-7057.
- Martin, A. and Pinkerton, A.A. (1998) Charge density studied using CCD detectors: Oxalic acid at 100 K revisited. *Acta Cryst B* 54, 471-477.
- Mendive, C.B., Bredow, T., Feldhoff, A., Blesa, M.A. and Bahnemann, D. (2009) Adsorption of oxalate on anatase (100) and rutile (110) surfaces in aqueous systems: Experimental results vs. theoretical predictions. *Phys. Chem. Chem. Phys.* 11, 1794-1808.

- Öhrström, L. and Michaud-Soret, I. (1999) Fe - Catecholate and Fe - Oxalate Vibrations and Isotopic Substitution Shifts from DFT Quantum Chemistry. *J Phys Chem A* 103, 256-264.
- Otte, K., Schmahl, W.W. and Pentcheva, R. (2013) DFT+ U study of arsenate adsorption on FeOOH surfaces: Evidence for competing binding mechanisms. *J. Phys. Chem. C* 117, 15571-15582.
- Perdew, J.P., Burke, K. and Ernzerhof, M. (1997) Errata: Generalized gradient approximation made simple. *Phys. Rev. Lett.* 78, 1396.
- Perdew, J.P.p., Burke, K. and Ernzerhof, M. (1996) Generalized Gradient Approximation Made Simple. *Phys. Rev. Lett.* 77, 3865-3868.
- Persson, P. and Axe, K. (2005) Adsorption of oxalate and malonate at the water-goethite interface: Molecular surface speciation from IR spectroscopy. *Geochim. Cosmochim. Acta* 69, 541-552.
- Rassolov, V.A., Ratner, M.A., Pople, J.A., Redfern, P.C. and Curtiss, L.A. (2001) 6-31G* Basis Set for Third-Row Atoms. *J. Comput. Chem.* 22, 976-984.
- Reichard, P.U., Kretzschmar, R. and Kraemer, S.M. (2007) Dissolution mechanisms of goethite in the presence of siderophores and organic acids. *Geochim. Cosmochim. Acta* 71, 5635-5650.
- Schwertmann, U. and Cornell, R.M. (2000) *Iron Oxides in the Laboratory*, 2nd, Completely Revised and Extended Edition ed. Wiley-VCH Weinheim, Germany.
- Scott, A.P. and L, R. (1996) Harmonic Vibrational Frequencies: An Evaluation of Hartree-Fock, Møller-Plesset Quadratic Configuration Interaction, Density Functional Theory, and Semi-Empirical Scale Factors. 100, 16502-16513.
- Shippey, T.A. (1980) Vibrational studies in aqueous solutions. *journal of molecular structure* 65, 71-86.
- Simanova, A.A., Loring, J.S. and Persson, P. (2011) Formation of ternary metal-oxalate surface complexes on α -FeOOH particles. *J. Phys. Chem. C* 115, 21191-21198.
- Situm, A., Rahman, M.A., Goldberg, S. and Al-Abadleh, H.A. (2016) Spectral characterization and surface complexation modeling of low molecular weight organics on hematite nanoparticles: Role of electrolytes in the binding mechanism. *Environmental Science: Nano* 3, 910-926.
- Sulzberger, B. and Laubscher, H. (1995) Reactivity of various types of iron(III) (hydr)oxides towards light-induced dissolution. *Mar. Chem.* 50, 103-115.
- Yoon, T.H., Johnson, S.B., Musgrave, C.B. and Brown, J.G.E. (2004) Adsorption of organic matter at mineral/water interfaces: I. ATR-FTIR spectroscopic and quantum chemical study of oxalate adsorbed at boehmite/water and corundum/water interfaces. *Geochim. Cosmochim. Acta* 68, 4505-4518.
- Young, A.G. and McQuillan, A.J. (2009) Adsorption/desorption kinetics from ATR-IR spectroscopy. Aqueous oxalic acid on anatase TiO₂. *Langmuir* 25, 3538-3548.

TABLES AND FIGURES

Table 1. Comparison of experimental and theoretical IR frequencies (cm^{-1}) of inner-sphere and outer-sphere bonding geometries of oxalate to lepidocrocite for molecular clusters.

Modes	experimental frequencies	theoretical frequencies					
		BTri(010)	BM(100)	MM(100)	HOS(010)	HOS(100)	OS
$\nu_s(\text{C-O})$	1275 ± 6	1252 (-23)	1281 (6)	-	-	-	-
$\nu_s(\text{C-O})$	1286 ± 4	-	-	1285 (-1)	1278 (-8)	1301 (15)	-
$\nu_a(\text{C-O})$	1308 ± 1	-	-	-	-	-	1286(-22)
$\nu_a(\text{C-O})$	1403 ± 4	1375 (-28)	1406 (3)	-	-	-	-
$\nu_a(\text{C-O})$	1422 ± 4	-	-	1418 (-4)	1415 (-7)	1457 (35)	-
$\nu_a(\text{C-O})$	1567 ± 7	-	-	-	-	-	1565 (-2)
$\nu_a(\text{C-O})$	-	-	-	1575*	1552	1569	-
$\nu_a(\text{C=O})$	1609 ± 18	-	-	1609 (0)	1604 (-5)	1585 (-24)	-
$\nu_a(\text{C=O})$	1641 ± 28	1626 (-15)	1632 (-9)	-	-	-	-
$\nu_a(\text{C=O})$	1664 ± 9	-	-	1641 (-23)	missing	missing	-
$\nu_a(\text{C=O})$	1684 ± 3	1673 (-11)	1683 (-1)	-	-	-	-
$\nu_a(\text{C=O})$	1712 ± 1	1686 (-26)	1698 (-14)	-	-	1711 (-1)	-
R^2		0.999	0.999	0.998	0.999	0.987	-
slope		1.014	0.959	0.959	1.002	0.915	-
y-intercept		-41.927	59.668	53.237	-9.149	134.409	-
average difference		20.3	6.9	7.3	6.5	25.7	-

Listed in the second column are the rounded means and standard deviations of the experimentally determined frequencies by Gaussian peak fitting of different data sets. Gaussian peaks assigned to S_{BM} are listed in red, Gaussian peaks assigned to S_{MM} in blue, and Gaussian peaks assigned to S_{OS} in green. Rounded differences between the mean experimental and the theoretical frequencies are given in parentheses. (*The frequency at 1575 cm^{-1} for MM was not used, because it is too close to the observed S_{OS} band at 1565 cm^{-1} and the absorbance at around 1575 cm^{-1} is too featureless for the assignment of an additional peak position).

Table 2. Calculated relative stability of “dry” surface model and adsorption energy (ΔE_{ads}) of “solvated” surface model (kJ mol^{-1}).

(010)	Relative Stability (dry)	Adsorption Energy (solvated)	(100)	Relative Stability (dry)	Adsorption Energy (solvated)
BTetra ₁	113	-	BB*	146	-
BTetra ₂	71	-	BB	314	-
-	-	-	BM'	100	-
BTri	0	+29	BM	0	-89
MB	163	-	MM	92	-98

$\Delta E_{\text{ads}} = E(\text{outer sphere}) - E(\text{inner sphere})$, a negative value favors adsorption.

Note: calculated ΔE_{ads} do not consider entropy changes with adsorption.

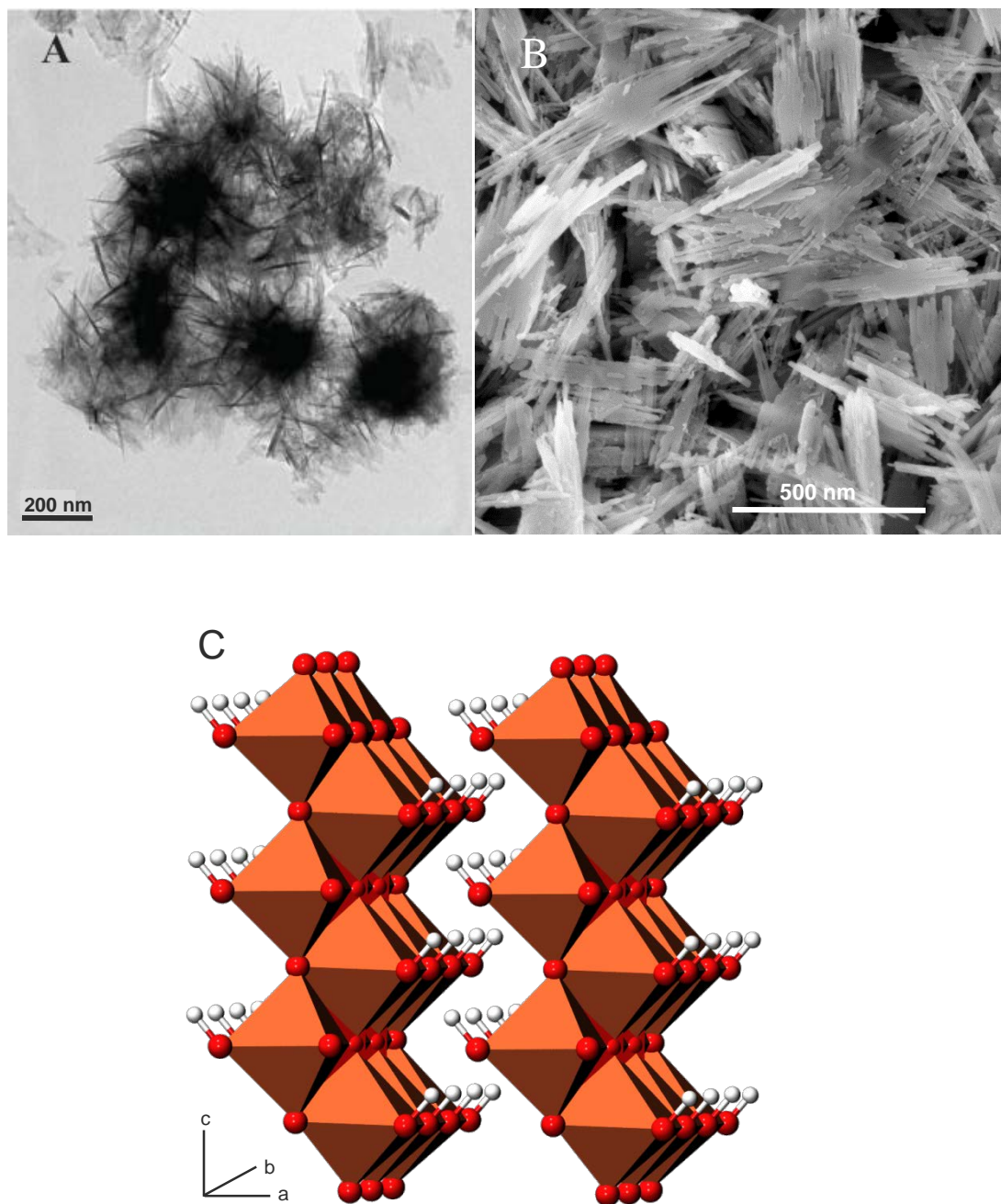


Figure 1. EM images of the lepidocrocite samples, and structure. (A) **Lp-1** prepared according to the method of [Brauer \(1963\)](#), TEM image adapted from [Borer et al. \(2009\)](#). (B) **Lp-2** synthesized according to [Schwertmann and Cornell \(2000\)](#). SEM image recorded on FEI Magellan 400, USA, with in-lens detector operated at 3kV. (C) Lepidocrocite structure with (100) surface in paper plane.

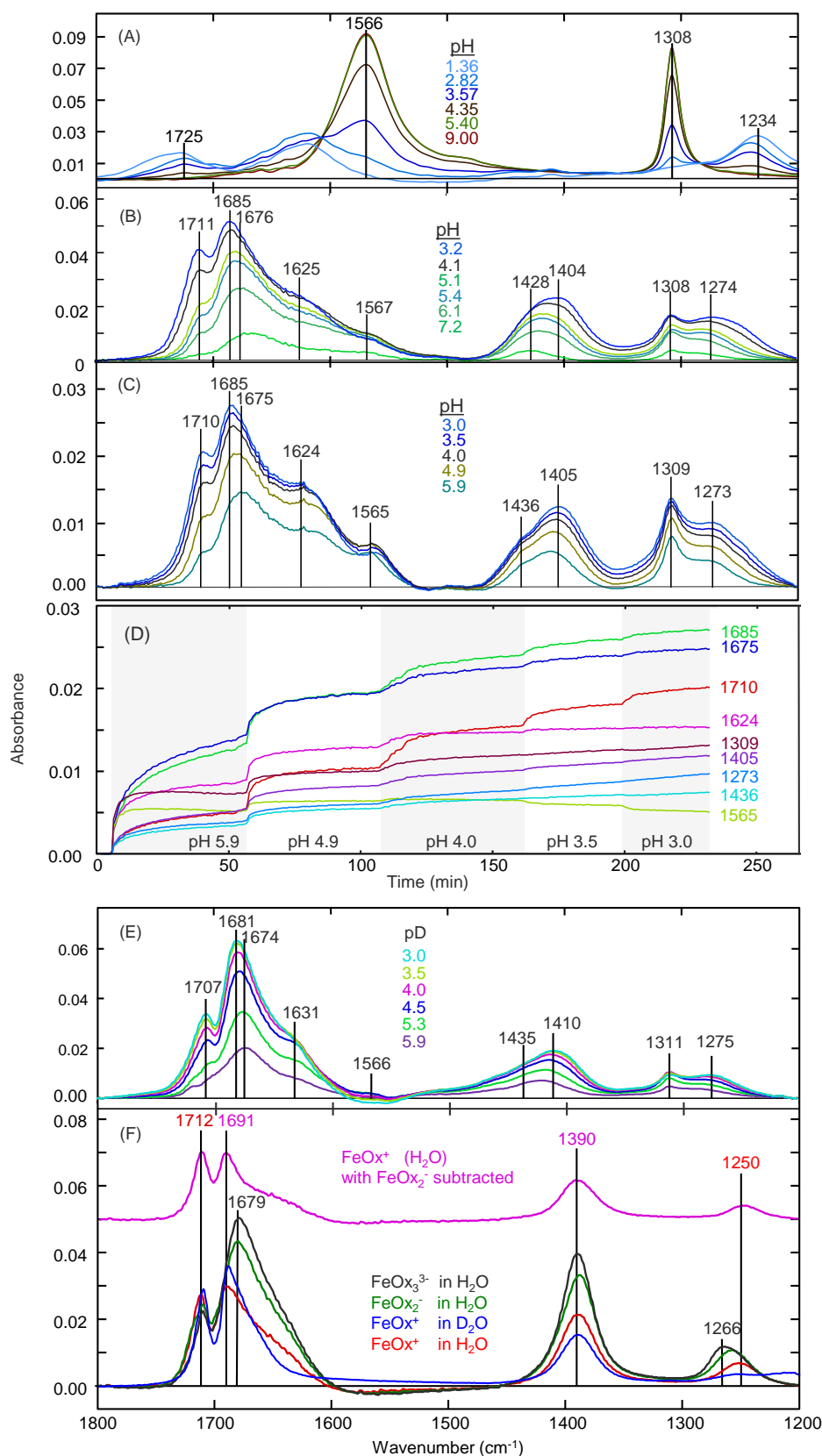


Figure 2. Background-subtracted ATR-FTIR absorbance spectra. (A) Aqueous solution of oxalic acid (50 mM) starting at pH 1.36 and titrated up to pH 9.00. (Adapted from Hug and Sulzberger (Hug and Sulzberger, 1994)). (B) and (C) Adsorption of aqueous oxalate (200 μM , $I = 10$ mM KCl) on **Lp-1** and **Lp-2**, respectively, at various pH values, close to equilibrium. (D) Kinetics of oxalate adsorption on **Lp-2** followed at different peak positions, as indicated in the plots (scans taken every 41.3 seconds). (E) Adsorption of oxalate on **Lp-2** in D_2O (200 μM , $I = 10$ mM NaCl) at pD 3.0-5.9. (F) Aqueous Fe-oxalate complexes as indicated in the figure, 10 mM in H_2O and 50 mM in D_2O , scaled to similar amplitudes at 1712 cm^{-1} .

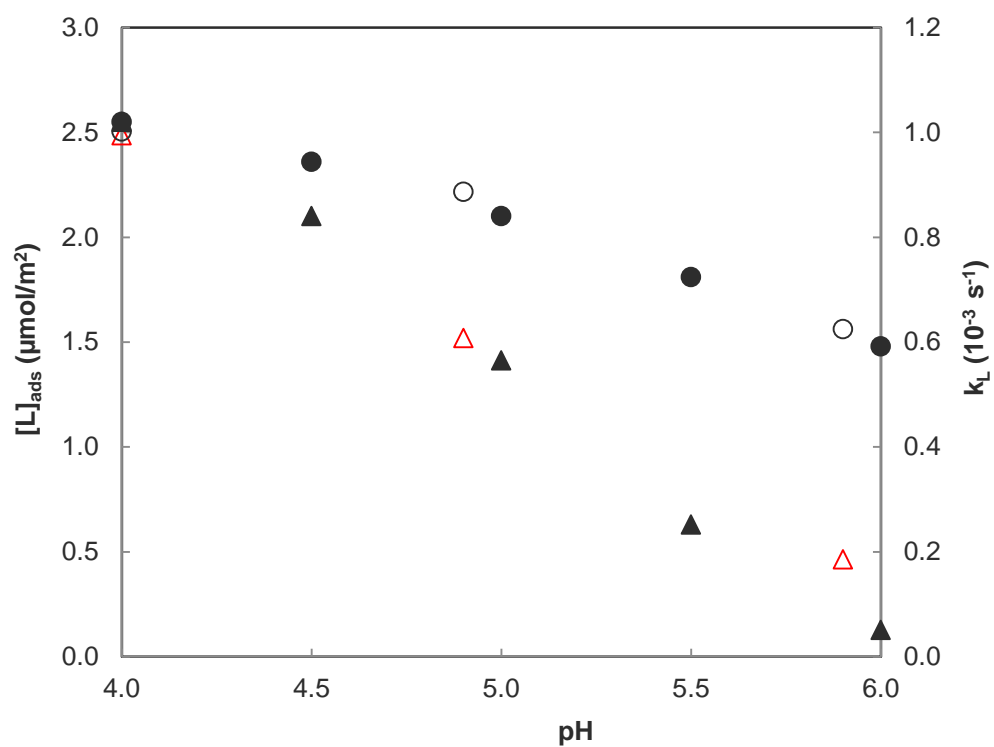


Figure 3. Effect of pH on adsorption of oxalate on Lp-2 (filled black circles, left y-axis) and rate coefficients (filled black triangles, right y-axis) of ligand controlled dissolution. Total oxalate concentrations were 500 μM in 0.01 M NaCl solution at solids concentrations of 0.1 g L^{-1} (adsorption and dissolution experiments). The empty red triangles show the contributions of BM and the empty black circles the sum of the contributions of BM, MM and OS, scaled to an amplitude of 2.5 $\mu\text{mol m}^{-2}$ at pH 4.0 for easier comparison.

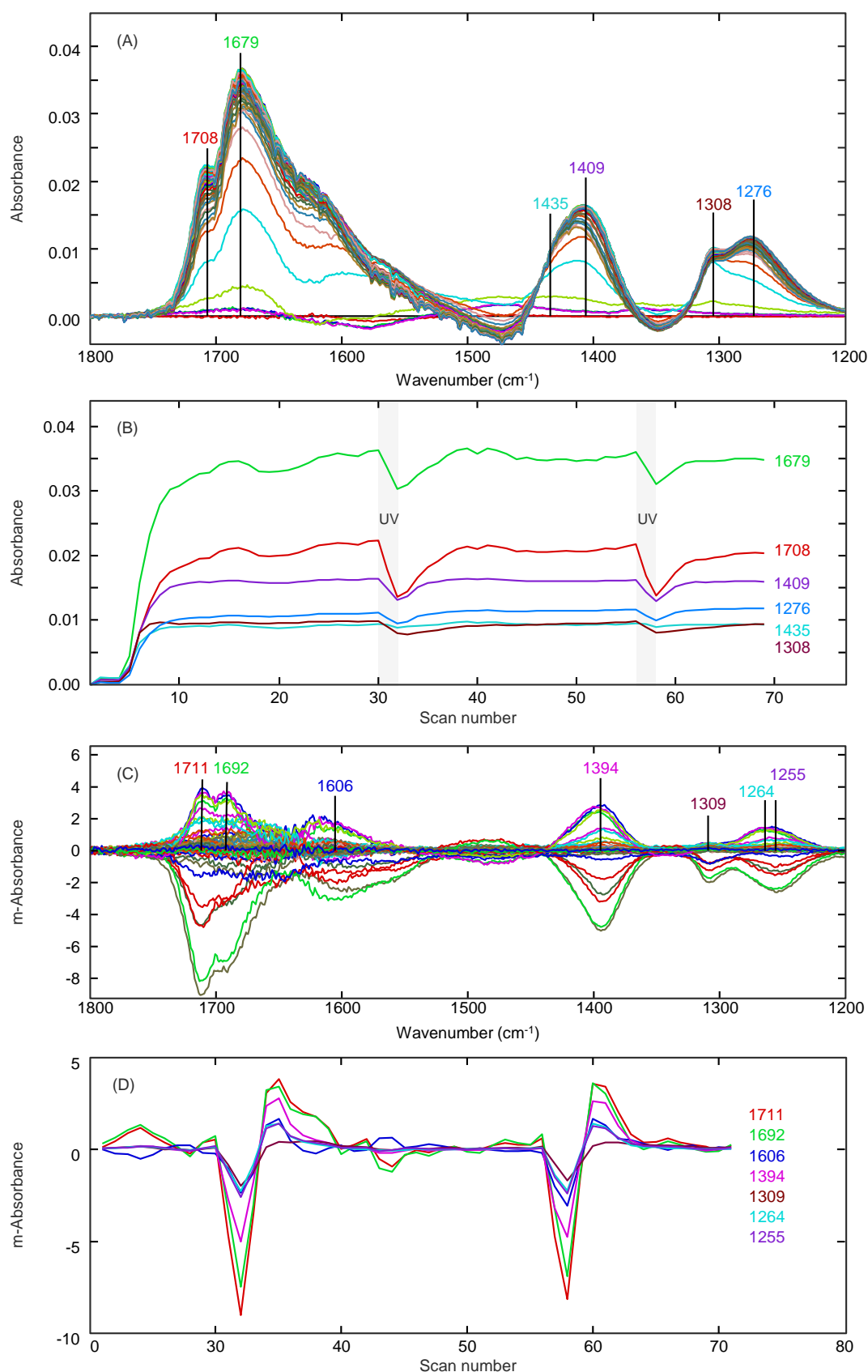


Figure 4. Adsorption of oxalate (200 μM) on **Lp-1** and illumination with 365 nm UV-light at pH 4.0. (A) Spectra during adsorption and illumination (scans every 71 seconds). (B) Kinetics measured at the wavelengths indicated. (C) Spectral differences during illumination (negative amplitudes) and during re-equilibration (positive amplitudes). (D) Kinetics of the differences at the wavelengths indicated as a function of time. The spectral differences in (C) resemble the spectral characteristics of FeOx^+ and of the Gaussian spectrum BM, while the changes in the spectral range of the MM-spectrum are much smaller. This indicates that the BM is the most photo-active surface complex.

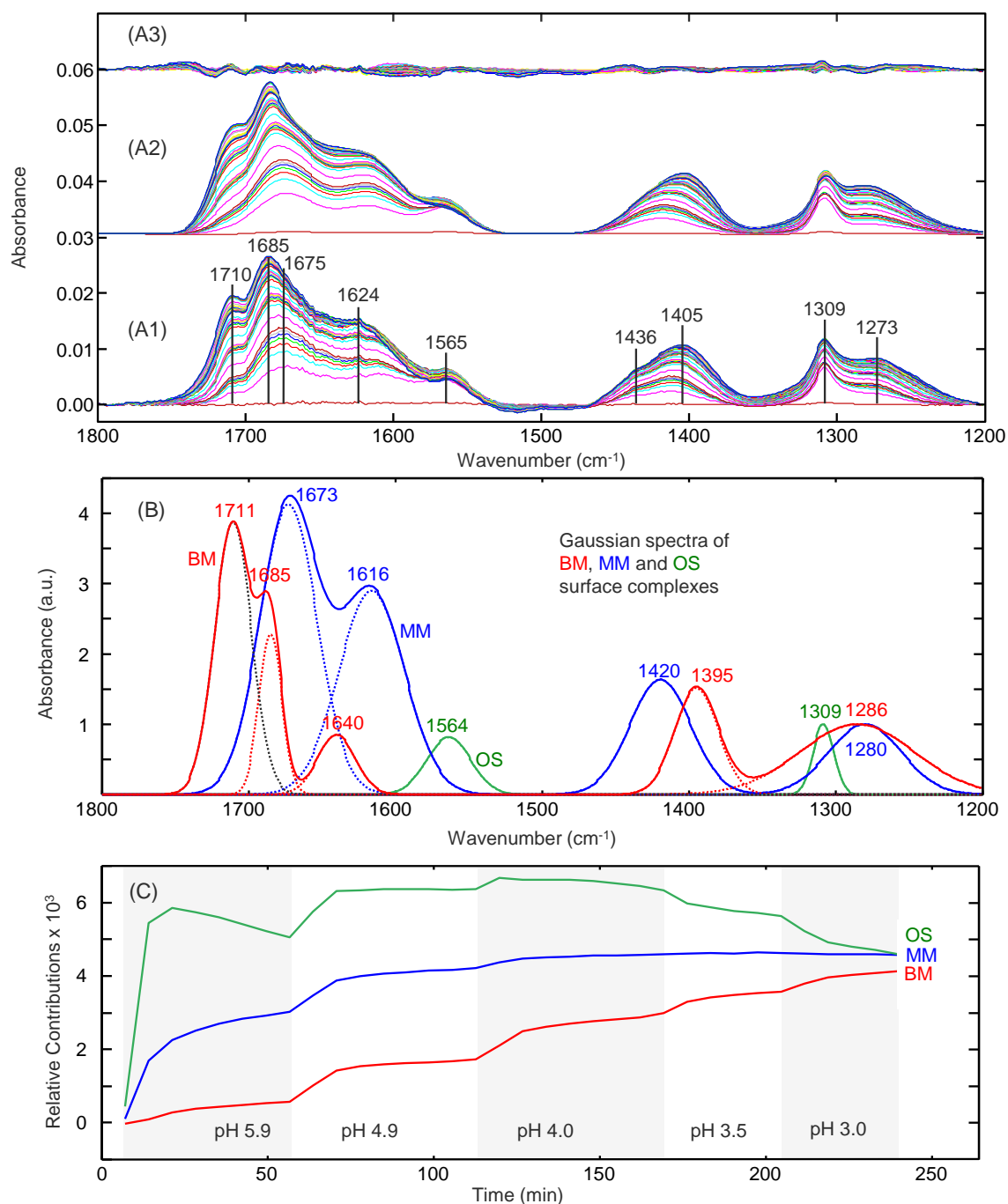


Figure 5. Adsorption of oxalate (200 μ M, I=10 mM NaCl) on **Lp-2** and spectral fits. (A1) Absorbance as a function of time and pH (spectra measured every 41.3 seconds). The data set is the same as in Figure 2 C, but spectra at more times are shown. (A2) reconstructed spectra with Gaussian line shapes (offset by 0.03 abs. units) and (A3) residuals (measured minus reconstructed spectra), offset by 0.06 abs. units. (B) Gaussian fits with five possible peaks for the spectrum of BM, four possible peaks for the spectrum of MM, and two possible peaks for the spectrum of OS. (C) Contributions of BM, MM, and OS as a function of time and pH.

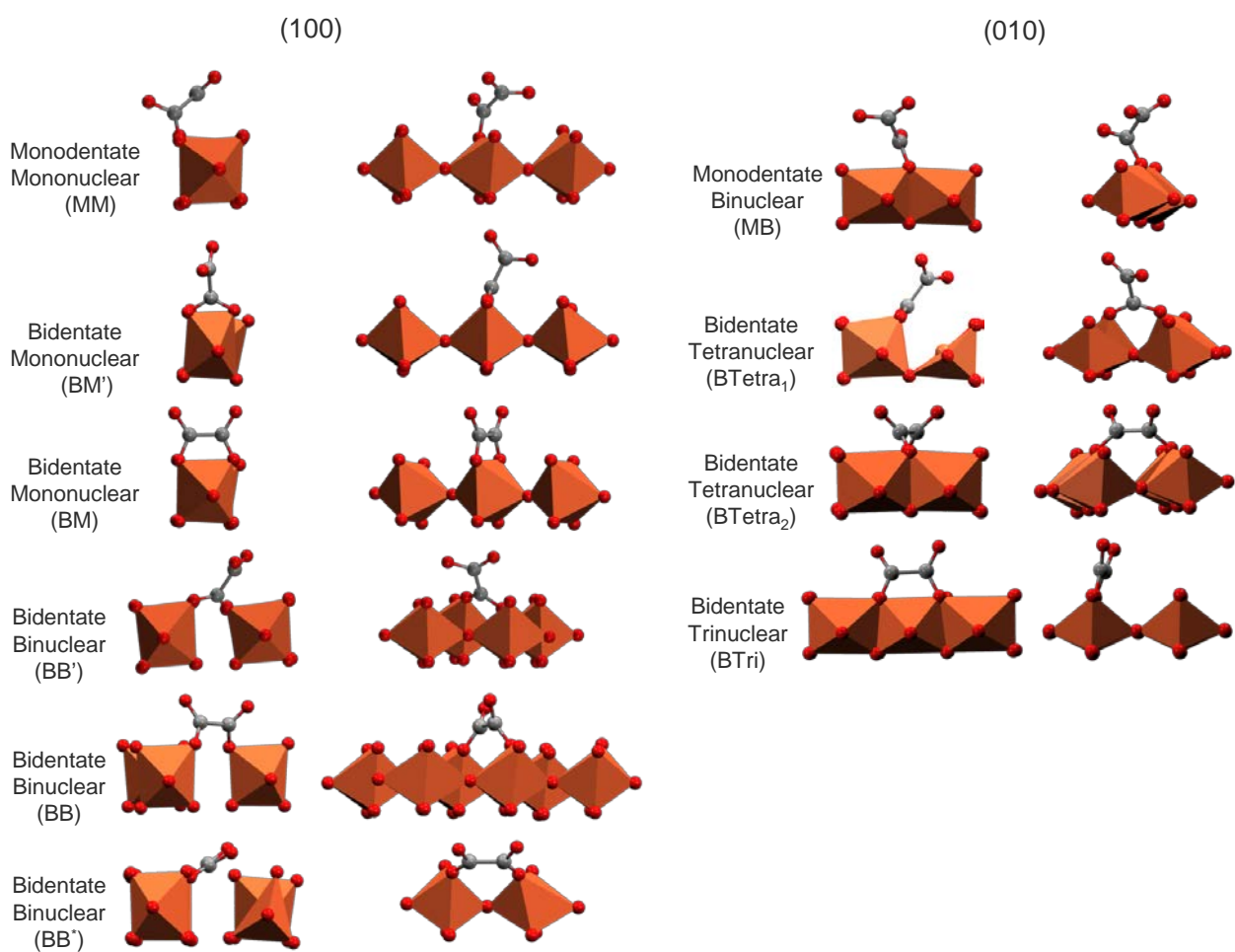


Figure 6. Possible bonding structures of oxalate adsorbed to lepidocrocite (010) and (100) surfaces. Fe atoms are represented by orange polyhedrons, O and C atoms are represented by red and gray spheres, respectively. H atoms are omitted.

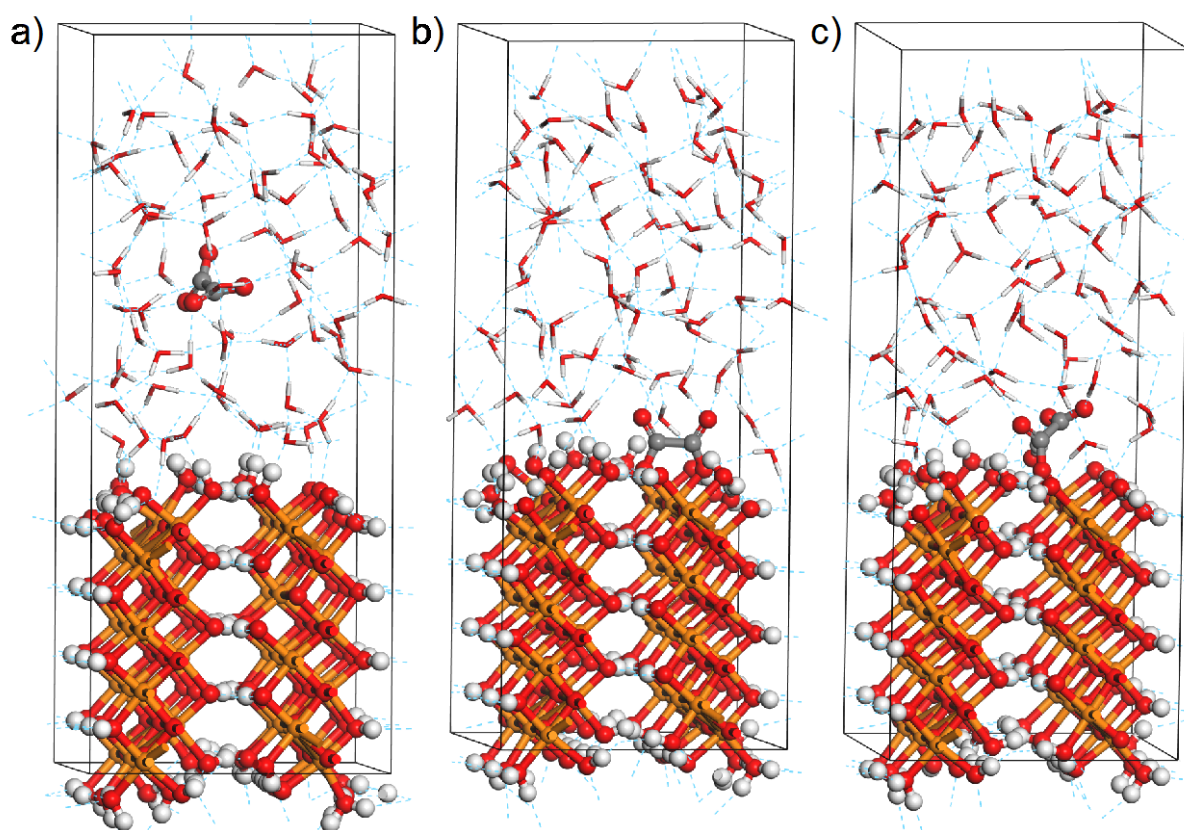


Figure 7. (a) Aqueous (OS), (b) BM, and (c) MM bonding configurations of “solvated” lepidocrocite (100) ($\text{Fe}_{48}\text{O}_{195}\text{H}_{240}\text{C}_2$). Fe, O, C, and H atoms are represented by orange, red, gray and white colors, respectively. The lepidocrocite layer is represented in a ball & stick style, while the hydrogen-bonded water molecules are represented in a licorice style. View with (001) surface in paper plane, looking down c-axis, 100 surface on top.

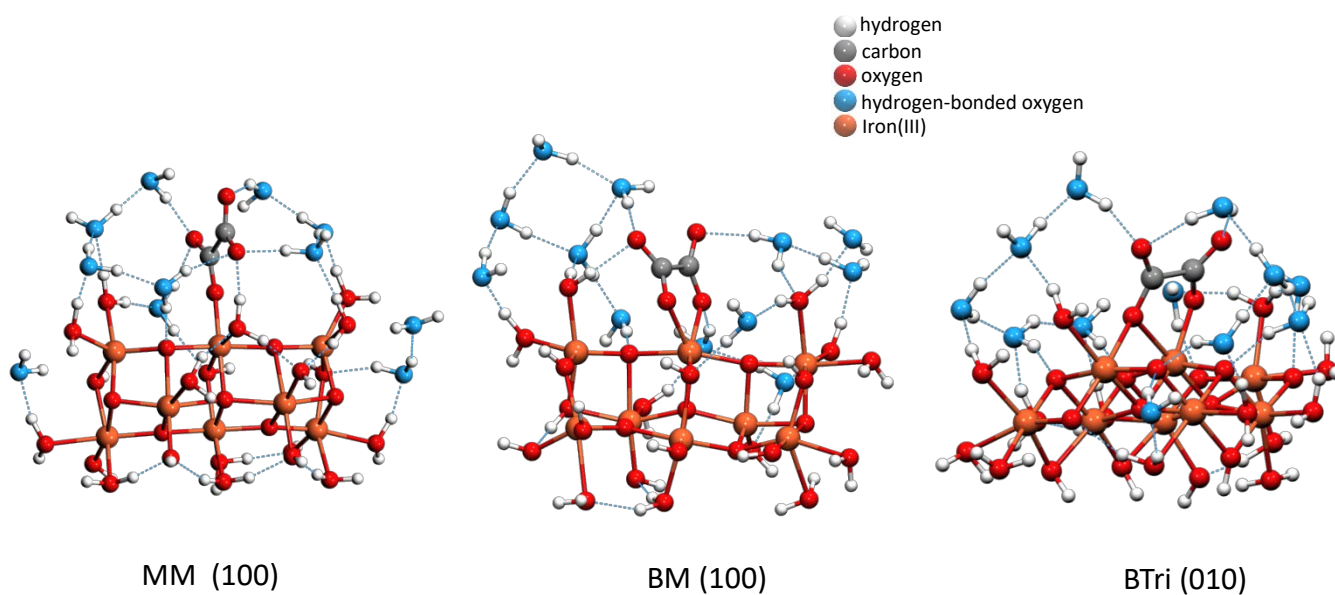


Figure 8. Geometry-optimized molecular clusters ($\text{C}_2\text{H}_{54}\text{O}_{42}\text{Fe}_8$) representing (010) and (100) surfaces, respectively, with MM, BM and BTri structures. Calculated at the B3LYP/6-31G(d,p) level in the gas phase.

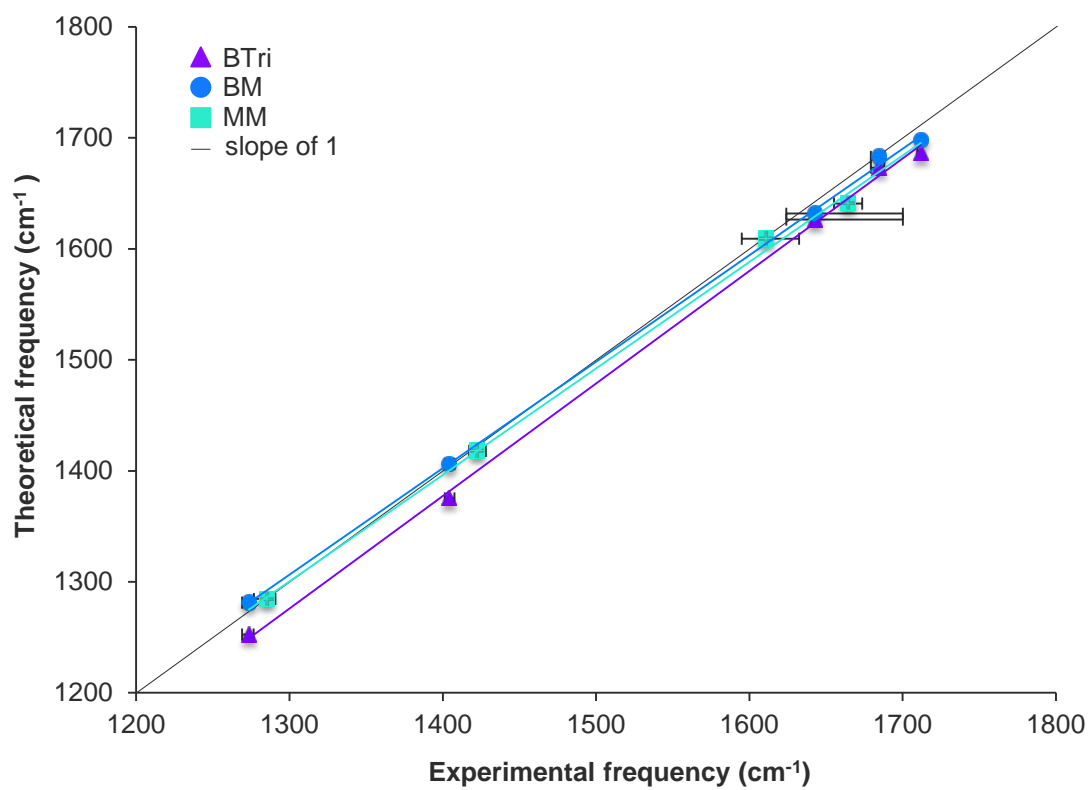


Figure 9. Linear regression comparison of experimental and theoretical frequencies of BTri, BM, and MM. Linear fit parameters are given in Table 1a.